Final analysis of ELAIS 15-μm observations: method, reduction and catalogue

Article (Published Version)

Mon. Not. R. Astron. Soc. **358,** 397–418 (2005) doi:10.1111/j.1365-2966.2005.08773.x

Final analysis of ELAIS 15-μm observations: method, reduction and catalogue

M. Vaccari,[1,2,3]★ C. Lari,[4] L. Angeretti,[5] D. Fadda,[6] C. Gruppioni,[7,8] F. Pozzi,[5] O. Prouton,[2] H. Aussel,[9] T. Babbedge,[1] P. Ciliegi,[8] A. Franceschini,[2] E. Gonzalez-Solares,[10] F. La Franca,[11] S. Oliver,[12] I. Perez-Fournon,[13] M. Rowan-Robinson,[1] S. Serjeant[14] and P. Väisänen[15,16]

[1]*Astrophysics Group, Blackett Laboratory, Imperial College, Prince Consort Road, London, SW7 2AZ*
[2]*Dipartimento di Astronomia, Università di Padova, Vicolo dell'Osservatorio 2, I-35122, Padova, Italy*
[3]*CISAS "G. Colombo", Università di Padova, Via Venezia 15, I-35131, Padova, Italy*
[4]*Istituto di Radioastronomia, CNR, Via Gobetti 101, I-40122, Bologna, Italy*
[5]*Dipartimento di Astronomia, Università di Bologna, Via Ranzani 1, I-40127, Bologna, Italy*
[6]*Spitzer Science Centre, MC 220-6, 1200 East California Boulevard, Pasadena, CA 91125, USA*
[7]*Osservatorio Astronomico di Padova, INAF, Vicolo dell'Osservatorio 5, I-35122, Padova, Italy*
[8]*Osservatorio Astronomico di Bologna, INAF, Via Ranzani 1, I-40127, Bologna, Italy*
[9]*Institute for Astronomy, University of Hawaii, 2680 Woodlawn Drive, Honolulu, HI 96822, USA*
[10]*Institute of Astronomy, University of Cambridge, The Observatories, Madingley Road, Cambridge, CB3 0HA*
[11]*Dipartimento di Fisica, Università di "Roma Tre", Via della Vasca Navale 84, I-00146, Roma, Italy*
[12]*Astronomy Centre, Department of Physics & Astronomy, University of Sussex, Brighton, BN1 9QJ*
[13]*Instituto de Astrofísica de Canarias, Via Lactea S/N, E-38200, La Laguna, Spain*
[14]*Centre for Astrophysics and Planetary Science, School of Physical Sciences, University of Kent, Canterbury, Kent, CT2 7NZ*
[15]*European Southern Observatory, Alonso de Cordova 3107, Casilla 19001 Santiago 19, Vitacura, Santiago, Chile*
[16]*Observatory, PO Box 14, FIN-00014, University of Helsinki, Helsinki, Finland*

Accepted 2004 December 22. Received 2004 December 21; in original form 2004 April 16

ABSTRACT

We present the final analysis of the European Large Area *Infrared Space Observatory* (*ISO*) Survey (ELAIS) 15-μm observations, carried out with the ISO Camera (ISOCAM) instrument on board the *ISO*.

The data-reduction method, known as the Lari Method, is based on a mathematical model of the behaviour of the detector and was specifically designed for the detection of faint sources in ISOCAM/ISO Photopolarimeter (ISOPHOT) data. The method is fully interactive and leads to very reliable and complete source lists.

The resulting catalogue includes 1923 sources detected with signal-to-noise ratio of > 5 in the 0.5–100 mJy flux range and over an area of 10.85 deg^2 split into four fields, making it the largest non-serendipitous extragalactic source catalogue obtained to date from the *ISO* data.

This paper presents the concepts underlying the data-reduction method together with its latest enhancements. The data-reduction process, the production and basic properties of the resulting catalogue are discussed. The catalogue quality is assessed by means of detailed simulations, optical identifications and comparison with previous analyses.

Key words: methods: data analysis – catalogues – galaxies: active – galaxies: evolution – galaxies: formation – infrared: galaxies.

1 INTRODUCTION

The *Infrared Astronomical Satellite* (*IRAS*, Neugebauer et al. 1984; Soifer, Houck & Neugebauer 1987) was extremely successful in characterizing for the first time the global properties of the mid- and far-infrared sky, carrying out an all-sky survey at wavelengths of 12, 25, 60 and 100 μm and leading to discoveries such as those of luminous, ultraluminous and hyperluminous infrared galaxies (LIRGs, ULIRGs and HLIRGs, respectively), a substantial population of evolving starbursts and the detection of large-scale structures in the galaxy distribution (Saunders et al. 1991).

★E-mail: m.vaccari@imperial.ac.uk

Unfortunately, the *IRAS* view was typically limited to the very local Universe ($z \lesssim 0.2$), thus hampering statistical studies of infrared-luminous galaxies at cosmological redshifts. Only few sources were detected by *IRAS* at higher redshifts, typically ULIRGs magnified by gravitational lenses, like F10214+4724 ($z = 2.28$, Rowan-Robinson et al. 1991). In particular only about 1 000 galaxies were detected all over the sky in the *IRAS* 12-μm band. Infrared source counts based on *IRAS* data (Rowan-Robinson et al. 1984; Soifer et al. 1984) showed some marginally significant excess of faint sources with respect to no evolution models (Hacking, Houck & Condon 1987; Franceschini et al. 1988; Lonsdale et al. 1990; Gregorich et al. 1995; Bertin, Dennenfeld & Moshir 1997), but not enough statistics and dynamic range in flux to discriminate between evolutionary scenarios were available.

Although conceived as an observatory-type mission, the *Infrared Space Observatory* (*ISO*, Kessler et al. 1996) was in many ways the natural successor to *IRAS*, bringing a gain of a factor ∼1000 in sensitivity and ∼10 in angular resolution in the mid-infrared. A substantial amount of *ISO* observing time was therefore devoted to field surveys aimed at detecting faint infrared galaxies down to cosmological distances. Such surveys were conceived as complementary in flux depth and areal coverage, allowing a systematic investigation of the extragalactic sky down to so far unattainable flux densities at both mid- and far-infrared wavelengths, whose results are summarized by Genzel & Cesarsky (2000). In particular, extragalactic 15 μm source counts determined with ISOCAM (Elbaz et al. 1999; Gruppioni et al. 2002) have revealed a significant departure from Euclidean slope within the 1–5 mJy flux range, which has been interpreted as evidence for a strongly evolving population of starburst galaxies.

The European Large Area *ISO* Survey (ELAIS, Oliver et al. 2000; Rowan-Robinson et al. 2004) was the most ambitious non-serendipitous survey and the largest Open Time project carried out with *ISO*, aimed at bridging the flux gap between *IRAS* all-sky survey and *ISO* deeper surveys. ELAIS observations mapped areas of about 12 deg^2 at 15 and 90 μm and smaller areas at 7 and 175 μm with the ISOCAM (Cesarsky et al. 1996, 7 and 15 μm) and ISOPHOT (Lemke et al. 1996, 90 and 175 μm) cameras. Most importantly, ELAIS 15-μm observations are the only ones allowing to sample the 1–5 mJy flux range, where most of the source evolution appears to take place.

Since the project approval, the ELAIS consortium, grown in time to a total of 76 collaborators from 30 European institutes, has undertaken an extensive program of ground-based optical and near-infrared imaging and spectroscopy. Thanks to such an extensive multiwavelength coverage, the ELAIS fields have now become among the best studied sky areas of their size, and natural targets of on-going or planned large-area surveys with the most powerful ground- and space-based facilities. Further details on ELAIS multiwavelength observations and catalogues are presented in Rowan-Robinson et al. (2004). After the loss of the *WIRE* satellite, notwithstanding the observations at several infrared wavelengths now coming from *Spitzer* and later from *SOFIA* and *Herschel*, *ISO* observations will remain a valuable data base for many years to come. In particular, until the advent of *ASTRO-F* (Shibai 2004) and *JWST*, ELAIS 15-μm observations will provide a complementary view on three areas (S1, N1 and N2) which will be covered at different wavelengths as part of the *Spitzer* Wide-Area Extragalactic Survey (SWIRE, Lonsdale et al. 2003). Thus the need of reducing such data with the uttermost care and providing the community with an agreed-upon legacy from the ELAIS project.

This paper presents the final analysis (FA) of the ELAIS 15-μm observations, and is structured as follows. In Section 2 a brief description of the most relevant aspects of the ELAIS 15-μm data set is given. Section 3 describes the data-reduction method and its improvements. In Section 4 the technique employed for flux determination and its results are presented. Section 5 details the results of the simulations that were carried out in order to assess the performance of the data-reduction method and thus the quality of the resulting catalogue. In Sections 7 and 8, respectively, estimates of the achieved astrometric and photometric accuracy are given. Section 6 summarizes the identification of 15-μm sources in optical and near-infrared images, while Section 9 describes the procedure adopted to establish the catalogue photometric calibration. Finally, Section 11 describes gives a basic description of the catalogue contents.

2 THE ELAIS 15-μm DATA SET

The ELAIS 15-μm main[1] data set is made up of 28 rasters (*ISO* basic imaging observations), each covering an area of about 40 arcmin×40 arcmin, divided into four fields – one (S1) in the southern hemisphere and three (N1, N2 and N3) in the northern one. Small superpositions at the boundaries and a limited degree of redundancy on portions of the fields give a total covered area of 10.85 deg^2.

The fields were selected on the basis of their high ecliptic latitude ($|\beta| > 40^\circ$, to reduce the impact of Zodiacal dust emission), low cirrus emission ($I_{100\,\mu m} < 1.5\,\mathrm{mJy}^{-1}$ sr) and absence of any bright ($S_{12\,\mu m} > 0.6$ Jy) *IRAS* 12-μm source. In Fig. 1 the location on the sky of the survey fields is shown, overlaid on cirrus maps [*COBE* normalized *IRAS* maps of Schlegel, Finkbeiner & Davis (1998)]. Nearby *IRAS* sources with 12-μm fluxes brighter than 0.6 Jy are also plotted. The overall sky coverage, highlighting the position and redundancy of single rasters, is illustrated in Fig. 2.

ELAIS 15-μm observations were carried out operating the ISOCAM instrument in raster mode using the long wavelength (LW) 3 filter. In this observing mode, the ISOCAM 32 × 32 pixel LW detector was stepped across the sky in a grid pattern, with about half detector width steps in one direction and the whole detector width steps in the other. Thus, reliability was improved as each sky position (apart from those at the boundaries of the raster region) was observed twice in successive pointings and overheads were reduced because each raster covered a large area (∼40 arcmin × 40 arcmin). At each raster pointing (i.e. grid position) the detector was read out several (typically 10) times, to increase the redundancy in order to be able to identify cosmic rays impacts and distinguish their severe effects on the electronics from real sources. Furthermore, on the raster first pointing, 80 readouts were carried out to allow the detector to approach stabilization. Table 1 describes the observation parameters for the LW3 observations, while Table 2 lists the fields and related *ISO* Data Archive filenames making up the data set.

3 DATA REDUCTION

Reduction of data obtained with *ISO* instrumentation has always proved very difficult for a number of reasons. As far as ISOCAM

[1] Note that smaller sky regions observed with an higher redundancy as part of the ELAIS project, such as the S2 field [whose data reduction and analysis is described by Pozzi et al. (2003)], the X1, . . . ,6 fields and the ultradeep portion of the N1 field, which was observed ten times, are not considered in this work. See Oliver et al. (2000) for further details on these smaller fields.

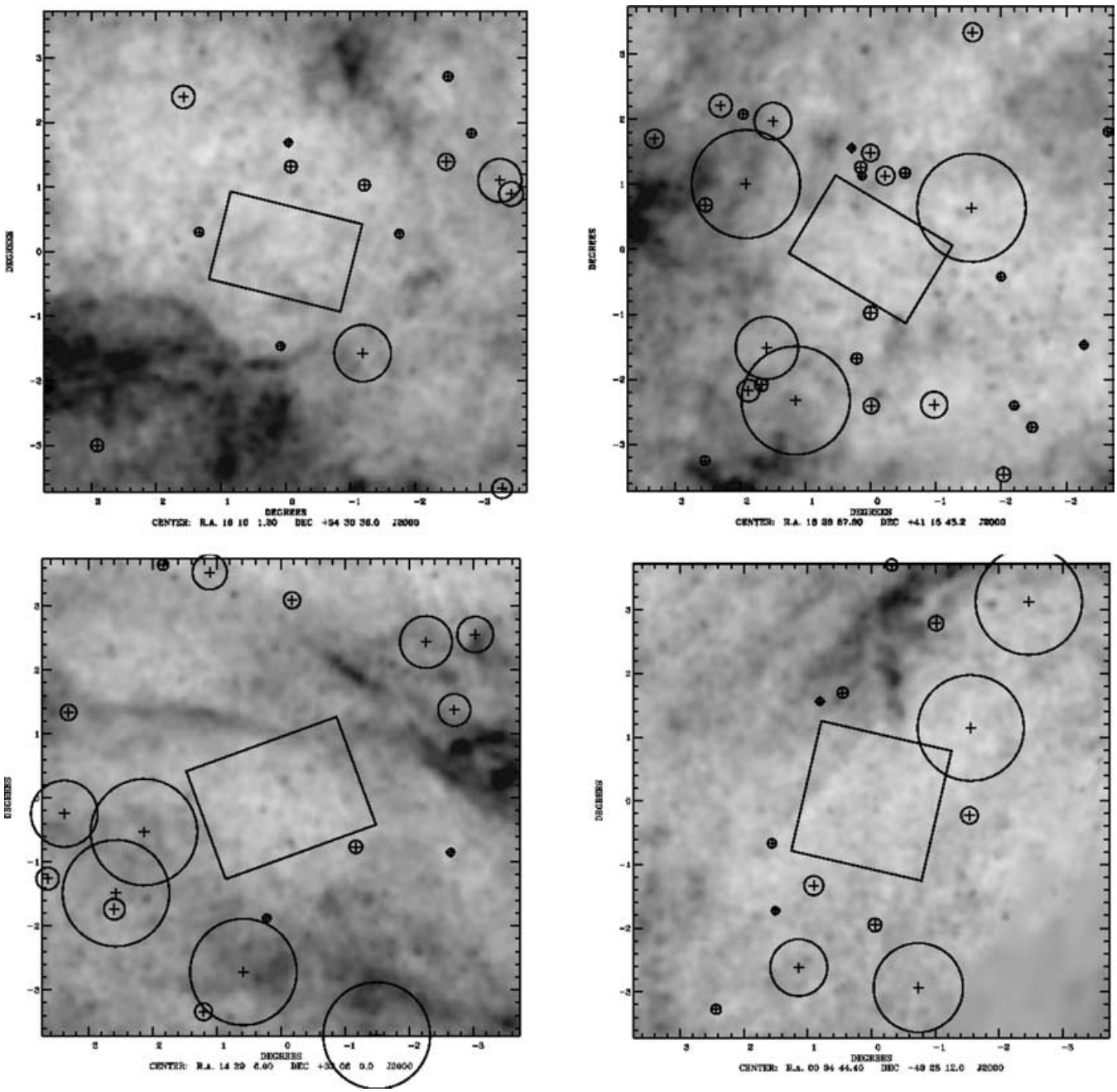

Figure 1. Sky locations of ELAIS 15-μm fields. From top left to bottom right: N1, N2, N3 and S1 areas. Grey-scales indicate *COBE* normalized *IRAS* 100-μm intensity maps from Schlegel et al. (1998), where a darker shade of grey means an higher brightness. *IRAS* sources with 12-μm fluxes brighter than 0.6 Jy are also drawn as circles with radii proportional to their fluxes.

observations carried out using the LW detector are concerned, the two most important instrumental phenomena one has to deal with are the qualitatively very different effects produced on the electronics of the detector by the frequent and severe cosmic ray impacts, which have long been known and referred to as **glitches**, and its sizeable transient behaviour after changes in the incident photon flux, which we will hereafter simply refer to as **transients**. In both cases, the cryogenic operational temperatures of the detector caused it to very slowly respond after these events. Lack of an accurate modelling of these effects can thus lead to spurious detections or errors in flux determination. In ELAIS 15-μm data reduction, the impact of these effects is increased by the instrumental parameters which were chosen in order to maximize the survey area. The short integration time (2.1 s × 10 frames per pointing), the large raster step (half the detector size along one axis and the whole detector size along the other one) and the large pixel size (6 arcsec) all contribute to reduce the redundancy and to increase the undersampling. Low redundancy and high undersampling, in turn, increase difficulties in distinguishing sources from strong glitches (low reliability) and in correctly determining source fluxes (low photometric accuracy).

Roughly speaking, glitches can be divided into three categories according to the way they shape the output signal of the detector, their decay time and influence on the pixel responsivity: glitches belonging to these different classes are respectively dubbed

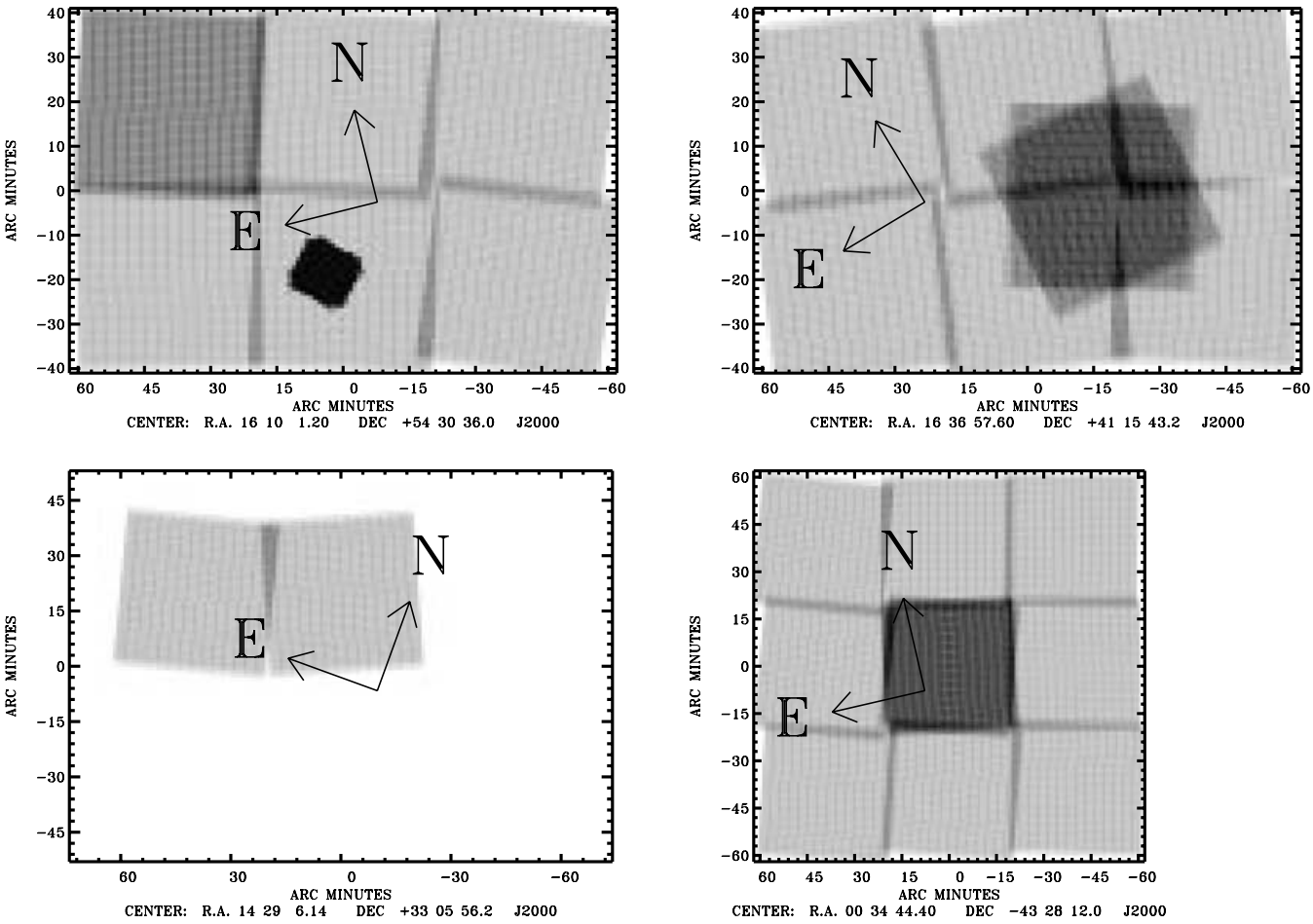

Figure 2. ELAIS 15-μm sky coverage. From top left to bottom right: N1, N2, N3 and S1 fields. Note that different fields are represented with a slightly different image scale.

common glitches, faders and **dippers**. Slow decreases of the signal following cosmic ray impacts are called faders, while prominent reductions of the pixel responsivity very slowly recovering afterwards are called dippers. These two effects are believed to be associated with proton or α particle impacts on the detector, and have a fairly long lasting impact on pixel responsivities. Conversely, the much more frequent impacts of cosmic ray electrons produce common glitches characterized by a relatively fast decay time, lasting only a few readouts. Therefore, the number of frames affected by a single fader or dipper is much higher than in the case of a common glitch, the pixel responsivity taking from tens to hundreds of seconds to recover completely. However, common glitches are much more frequent than faders and dippers and, may all the same hamper the quality of data reduction. Thus, all kinds of glitches, if not correctly removed (or, more properly, corrected for), can lead to spurious detections, or **unreliability**, and to the loss of genuine sources, or **incompleteness**. On the other hand, transients all follow the same pattern, owing to the fact that they arise from the non-negligible time it takes for the output signal to reach the stabilization value after a change in the incident photon flux has taken place. The measured signal is thus always lower than the true one. Failing to model this time effect in data reduction can lead to a systematic underestimation of source fluxes. For these reasons, the data cleaning and modelling is an extremely delicate process requiring great care in order to produce highly reliable sky maps and source lists.

Table 1. ELAIS ISOCAM LW3 observation parameters.

Parameter	Value
Band $\lambda_{\rm eff}$	14.3 μm
Band FWHM Range	12.0–18.0 μm
Detector gain	2[a]
Integration time	2 s
Number of exposures per pointing	10
Number of stabilization exposures	80
Pixel field of view	6 arcsec
Number of pixels	32 × 32
Number of horizontal and vertical steps	28 , 14
Number of rasters (including repetitions)	28
Horizontal and vertical step sizes	90 arcsec, 180 arcsec
Total area	10.85 deg^2

[a]Except in 'test' raster N2_R_A where gain was 1.

While it was variously demonstrated that it is possible, at least to a certain extent, to describe the behaviour of the detector by adopting some physical model, the large number of readouts involved in raster observations and the peculiar nature and strength of noise patterns also require efficient and robust algorithms to be developed so as to make the actual data reduction undertaking feasible in a nearly automatic way.

Table 2. ELAIS 15-μm fields. Field name, raster name, *ISO* data archive (IDA) official filename and raster centre coordinates.

Field	Raster	IDA	RA (J2000)	Dec. (J2000)
S1	S1_1	23200251	00 30 25.40	−42 57 00.3
	S1_2	23200353	00 31 08.20	−43 36 14.1
	S1_3	41300955	00 31 51.90	−44 15 27.0
	S1_4[a]	23300257[a]	00 33 59.40	−42 49 03.1
	S1_5_A	23300459	00 34 44.40	−43 28 12.0
	S1_5_B	77500207	00 34 44.40	−43 28 12.0
	S1_5_C	78502406	00 34 44.40	−43 28 12.0
	S1_6[b]	41001161[b]	00 35 30.40	−44 07 19.8
	S1_7	40800663	00 37 32.50	−42 40 41.2
	S1_8	40800765	00 38 19.60	−43 19 44.5
	S1_9	41001867	00 39 07.80	−43 58 46.6
N1	N1_1	30200101	16 15 01.00	+54 20 41.0
	N1_2_A[c]	30400103[c]	16 13 57.10	+54 59 35.9
	N1_2_B	67200103	16 13 57.10	+54 59 35.9
	N1_3	30500105	16 10 34.90	+54 11 12.7
	N1_4	30600107	16 09 27.00	+54 49 58.7
	N1_5	31000109	16 06 10.80	+54 01 08.0
	N1_6	30900111	16 04 59.00	+54 39 44.3
N2	N2_1	50200119	16 32 59.80	+41 13 33.2
	N2_2	51100131	16 34 44.50	+40 38 45.0
	N2_3	50000723	16 36 05.50	+41 33 11.8
	N2_4	50200225	16 37 48.90	+40 58 13.1
	N2_5	50100727	16 39 13.80	+41 52 31.6
	N2_6	50200429	16 40 55.50	+41 17 22.7
	N2_R_A	11600721	16 35 45.00	+41 06 00.0
	N2_R_B	77900101	16 35 45.00	+41 06 00.0
N3	N3_3	42500237	14 29 38.30	+33 24 49.6
	N3_5	43800341	14 32 38.20	+33 11 10.3

[a]Originally flagged as 'telemetry drops' in observation logs.
[b]Originally flagged as 'unknown quality' in observation logs.
[c]Originally flagged as 'aborted' in observation logs.

A number of data-reduction methods has thus been developed and tested, mostly on deep fields [e.g. the PRETI method by Starck et al. (1999) and the Triple Beam Switch method by Désert et al. (1999)]. Unfortunately, such methods did not prove satisfactorily reliable on shallower fields, leading to a high number of false detections. In addition, they suffered from the lack of an efficient way to interactively check the quality of the data reduction when needed. The Preliminary Analysis of ELAIS 15-μm data (Serjeant et al. 2000) was thus carried out adopting a more traditional approach involving the corroboration of automated detections through visual inspection by different observers.

The data reduction described in this paper was carried out using the Lari Method (Lari et al. 2001, 2003), a new technique developed to overcome these difficulties and provide a robust interactive technique for the reduction and analysis of ISOCAM and ISOPHOT data, particularly suited for the detection of faint sources and thus for the full exploitation of their scientific potential. The method was variously refined, and significantly better results are now obtained, with respect to the technique used in Lari et al. (2001) for the reduction of the S1 field, so that a thorough re-reduction of all ELAIS fields seemed appropriate and was thus carried out. As before, data reduction is carried out within an Interactive Data Language (IDL) environment using mostly purpose-built routines, exploiting CAM Interactive Analysis (CIA, Ott et al. 2001) software for basic operations only.

3.1 The Model

The Lari Method describes the sequence of readouts, or time history, of each pixel of ISOCAM LW3 detector in terms of a mathematical model for the charge release towards the contacts. Such a model is based on the assumption of the existence, in each pixel, of two charge reservoirs, a short-lived one Q_b, also known as **breve**, and a long-lived one Q_l, also known as **lunga**, evolving independently with a different time constant and fed by both the photon flux and the cosmic rays. The model is fully charge conservative, i.e. no decay of accumulated charges is considered, except towards the contacts, and thus the observed signal S is related to the incident photon flux I and to the accumulated charges Q_b and Q_l by

$$S = I - \frac{\mathrm{d}Q_\mathrm{tot}}{\mathrm{d}t} = I - \frac{\mathrm{d}Q_\mathrm{b}}{\mathrm{d}t} - \frac{\mathrm{d}Q_\mathrm{l}}{\mathrm{d}t}, \tag{1}$$

where the evolution of these two quantities is governed by the same differential equation, albeit with a different efficiency e_i and time constant a_i

$$\frac{\mathrm{d}Q_i}{\mathrm{d}t} = e_i\, I - a_i\, Q_i^2 \quad \text{where } i = \mathrm{b}, \mathrm{l}, \tag{2}$$

so that

$$S = (1 - e_\mathrm{b} - e_\mathrm{l})\, I + a_\mathrm{b}\, Q_\mathrm{b}^2 + a_\mathrm{l}\, Q_\mathrm{l}^2. \tag{3}$$

In other words, the variation in the accumulated charges is made up by two contributions, one increasing the reservoir and arising from the incident photon flux ($e_i\, I$) and one decreasing the reservoir and arising from the accumulated charges which are released towards the contacts ($-a_i\, Q^2$). In the ideal case of a detector with no memory effects e_i would be null and charges would not be accumulated within the pixels of the detector but instantly released towards the contacts. The values of the parameters e_i and a_i depend on the physics of the detector, and are found to depend on the exposure time t of a given observation and on the stabilization background level B of a given pixel, according to the relation

$$a_i = \frac{t}{t_0}\sqrt{\frac{B}{B_0}}\, a_{i,0}, \tag{4}$$

where $a_{i,0}$ is the value of a_i relative to a reference exposure time t_0 and stabilization background level B_0. Apart from this scaling, the same values for the e_i and a_i parameters are used for all pixels. This same scaling scheme was successfully applied to ISOCAM observations spanning a wide range of background levels and exposure times (Fadda et al. 2004; Rodighiero et al. 2004) and was applied to ISOPHOT observations as well (Rodighiero et al. 2003). In practice, an additive offset signal attributable to thermal dark current (a component which is otherwise removed in standard dark current subtraction), is actually added to both S and I in the relations above when it is estimated to be important, i.e. in the rare cases when the deepest dippers' depth otherwise exceeds 10 per cent of the stabilization background level.

3.2 Pipeline

Data reduction begins with a preliminary **pipeline** incorporating all necessary steps in order to prepare the data for the temporal fitting procedure which is the critical step of the Lari Method.

Raw data downloaded from the *ISO* Data Archive are first imported into the IDL `raster` structure containing all observational information using CAM interactive analysis (CIA) routines. Likewise, dark current subtraction and conversion from analogue to digital unit (ADU) to $\mathrm{ADU}^{-1}\ \mathrm{gain}^{-1}\ \mathrm{s}^{-1}$ are carried out using CIA. Then a dedicated IDL structure called `liscio` is built in order to contain not only all `raster` information but also all ancillary arrays needed in order to carry out the following reduction.

At this stage potential glitches are identified through a two-step five-point median filtering process of each pixel time history, or **deglitching**. In the first step, dealing with the strongest glitches, departures between data and median-filtered data greater than 7.0 $\mathrm{ADU^{-1}\ gain^{-1}\ s^{-1}}$ (about 35 times the typical rms noise) are flagged. In the second step, dealing with more common glitches, previously flagged readouts are masked and departures greater than 0.7 $\mathrm{ADU^{-1}\ gain^{-1}\ s^{-1}}$ (about 3.5 times the typical rms noise) are further flagged. The height of glitches is also stored as the difference between data and median-filtered data.

Then a separate routine determines the stabilization background (or global background, as opposed to the local background described below) and the aforementioned offset signal. Such a routine is carefully devised to filter out in so far as possible long-term effects such as stabilization, faders and dippers and thus provide a reliable estimate of the background and the offset, as the fitting procedure is particularly sensitive to them. The same routine also identifies the few potential bright sources which at times the fit failed to recognize by itself, which are then interactively checked to assess their reliability.

3.3 Fitting

The signal as a function of time is finally processed independently for each pixel. The fitting procedure models the transients attributable to changes in incident flux and the features on both short and long time-scales produced by cosmic ray impacts on the time history, modelling glitches as discontinuities in the charge release. As seen in Section 3.1, the same values for the e_i and a_i parameters are used for all pixels, apart from the scaling of the a_i according to the exposure time and the stabilization background level, leaving as free parameters only the charges at the beginning of the observation and at the 'peaks' of glitches.

When fitting the time history of a given pixel, all potential glitches identified for that pixel above the aforementioned 0.7 $\mathrm{ADU^{-1}\ gain^{-1}\ s^{-1}}$ threshold are acceptable to the fitting routine. Glitches from nearby pixels are also considered when their height is substantially (i.e. 20 times) higher than the chosen threshold. The fitting algorithm starts with the strongest potential glitches identified in pipeline deglitching, assumes discontinuities at these positions and tries to find a fit to the time history that satisfies the model assumed to describe the solid-state physics of the detector. If no acceptable fit is found, the next fainter glitch is considered as a potential discontinuity, and so on. Iteration of the fitting procedure is interrupted when either a satisfactory (typically 0.2 $\mathrm{ADU^{-1}\ gain^{-1}\ s^{-1}}$) data-model rms deviation is achieved or the maximum number of allowed iterations is reached.

At this stage the code estimates several quantities needed to build the sky maps on which source extraction will then be performed. All of these quantities are 'recovered' from glitches, i.e. already take into account discontinuities in charge release assumed to describe glitches during fit, and their list includes the following.

(i) The charges stored into the **breve** and **lunga** reservoirs at each readout.

(ii) The local background, i.e. the signal to be expected on the basis of the previously accumulated charges if only a photon flux equal to the stabilization background level, with no contribution from individual sources, was hitting the detector.

(iii) The model signal, produced by the incident flux coming from both the stabilization background and the detected sources.

(iv) The **'unreconstructed'** signal, i.e. the detected flux recovered from glitches but not from transients. This is computed as the difference between the measured signal and the local background.

(v) the **'reconstructed'** signal, i.e. the detected flux recovered not only from glitches but also from transients associated with changes in incident flux. This is computed from unreconstructed signal and charges through equation (1).

For the sake of clarity, one must emphasize here the differences between the two kinds of signals (and the corresponding fluxes and sky maps they will finally turn into) defined above, namely **unreconstructed** and **reconstructed** signals. Both quantities take into account the effects of the stabilization background and glitches on the detector, and the difference between their values is thus expected to be negligible if a source is not illuminating the pixel at the given pointing. The difference between the two quantities only appears when an additional signal the code is not able to model otherwise (i.e. as the effect of a glitch) is detected and attributed to a source of a given flux. The code then models the transients expected from such an additional flux and 'reconstructs' the signal one would detect if they did not affect the detector, i.e. if its response were instantaneous. In other words, unreconstructed signals do not take into account the effects of this modelling of changes in incident flux, thus representing the effective charge collected during the exposure, whereas reconstructed signals recover the charge 'loss' owing to the slow detector response. Therefore, the former are systematically lower than the latter. Actually, simulations show that the code is not actually able to properly model transients below a certain intensity threshold, thus suggesting the use of unreconstructed signals only to carry out further processing.

Fig. 3 shows how a successful fit is able to describe cosmic ray-induced violent changes in the signal level and thus recover useful information (specifically, source fluxes) from the pixel time history. Panels (a) and (b) show two examples of how glitches (a fader and a dipper, respectively) are described as discontinuities in the signal level slowly recovering towards the stabilization background, while panels (c) and (d) show how sources are detected even on the top of strong glitches. The solid line represents the observed data, the short-dashed line the best-fitting model and the long-dashed line the detected (unreconstructed) flux. The dot-dashed line finally represents the stabilization background.

It must be emphasized how in all of these cases the same mathematical model obeying the same equation with the same set of constants is able to successfully describe sources and glitches of very different shapes and strengths.

3.4 Interactive analysis

After running the fitting procedure on the time history of all pixels making up a raster, the interactive analysis of fitting results is carried out, looking in detail at portions of the time history that were not well fitted by the automated analysis. The details of the interactive analysis process need to be tuned to the quality of the specific raster under consideration. In particular, the choice of thresholds in interactive checks is closely related with observing parameters such as the exposure time but also with the varying frequency and severeness of cosmic ray impacts. Generally speaking, deeper checks could be profitably and time-effectively carried out on intrinsically higher-quality data, whereas noisy rasters would require spending a lot of time in interactive analysis to lower the adopted thresholds with dubious results. On the other hand, it is desirable to ensure as uniform a data reduction as practicable. The thresholds at which to perform interactive checks were therefore determined on the basis of

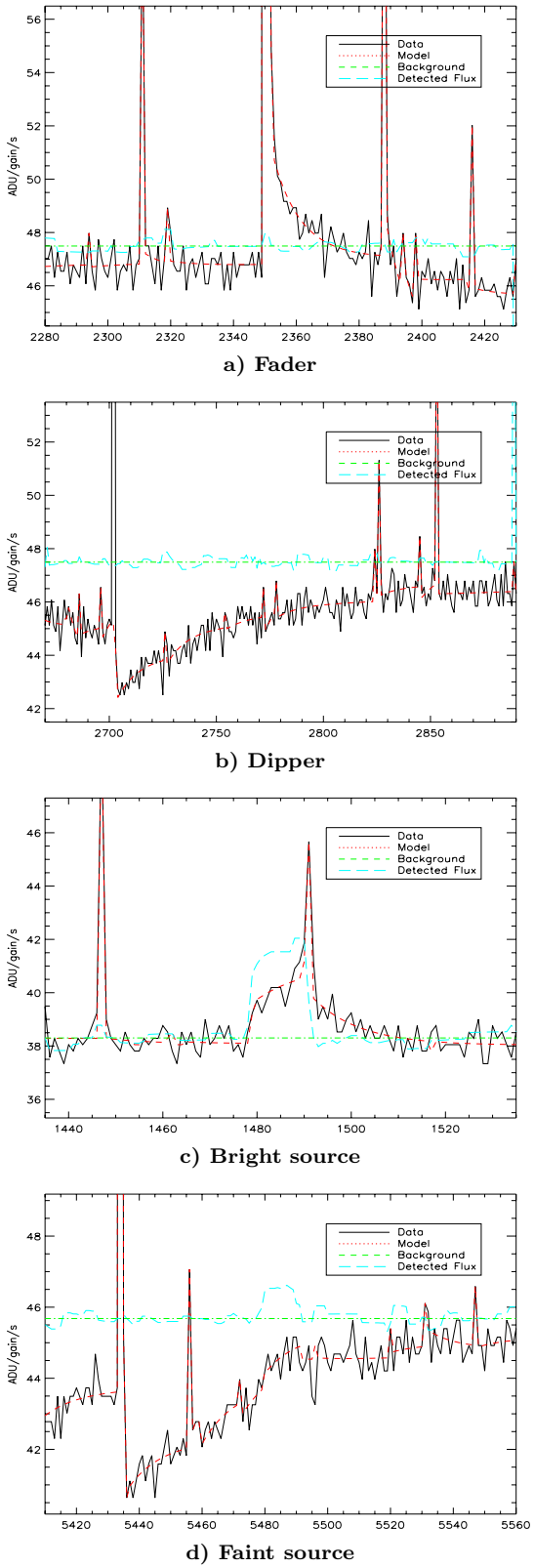

Figure 3. Different troublesome situations in pixel time histories: (a) Recovery of stabilization background level after a fader. (b) Recovery of stabilization background level after a dipper. (c) Detection of a bright source hidden by a strong common glitch. (d) Faint source hidden by the recovery of the stabilization background level after a dipper. 'Data' is the measured signal, 'Model' the modelled signal, 'Background' the stabilization background and 'Detected Flux' the reconstructed flux.

the balance between average data quality and time required by interactive analysis and then applied to all rasters.

As a first step, fitting failures flagged by substantial data-model rms deviations (higher that 0.23 $\mathrm{ADU^{-1}\,gain^{-1}\,s^{-1}}$) or negative signals (lower than -0.6 $\mathrm{ADU^{-1}\,gain^{-1}\,s^{-1}}$) are checked. Then all sizeable signal excesses (unreconstructed signals higher than 0.5 $\mathrm{ADU^{-1}\ gain^{-1}\ s^{-1}}$) are individually inspected. Whenever the need arises, a further fit extending to the whole pixel time history or to a smaller portion of it is carried out. Particularly noisy regions or very strong individual features completely preventing data reduction are masked.

The massive work of interactive analysis is carried out with an easy-to-use IDL widget-based Graphical User Interface, a screenshot of which is shown in Fig. 4, which allows any kind of operation that could be necessary: data visualization and browsing, glitch addition and correction, time history masking and re-fitting. Interactive analysis was already an integral part of the method used by Lari et al. (2001) as well, but the development of this piece of software enables us to apply it in a fuller way and thus increase the size and quality of the obtained catalogues. The ability to quickly flag and fit otherwise misdescribed cosmic ray or noise features allows us to lower the overall noise along the pixel time histories and thus enhance the signal-to-noise (S/N) ratio of sources. This is particularly important for faint sources, as many of them will have a S/N ratio which is very near to the catalogue threshold. Thus, even if the adopted S/N ratio catalogue threshold is the same as in Lari et al. (2001), we are now able to detect significantly more sources. At the same time, the bias that might be introduced by visual inspection is carefully reproduced in the simulations that are used to estimate the quality of data reduction, and is thus believed to be under control.

3.5 Mapping

Once a satisfactory fit is obtained over the whole time history for all pixels, one can proceed to the generation of sky maps and to source extraction. After masking glitches and other noisy parts of the time history identified during interactive analysis, flat-fielding is carried out by computing the median value of reconstructed signal along each pixel and rescaling signals from different pixels for this effect, then a flux estimate for each raster pointing is computed by averaging all readouts relative to that pointing. The result is converted from $\mathrm{ADU^{-1}\,gain^{-1}\,s^{-1}}$ to mJy using ISOCAM LW3 standard sensitivity $1\,\mathrm{mJy} = 1.96\,\mathrm{ADU^{-1}\,gain^{-1}\,s^{-1}}$. The 'images' thus computed relative to all raster pointings are then projected on to a 2 arcsec × 2 arcsec pixel sky map adopting nominal astrometric information and using a new mapping technique optimized to partly overcome the severe point spread function (PSF) undersampling owing to the large pixel size adopted in observations. Here and in the following, all necessary projections are carried out using the `projection` C++ code included in CIA. In so doing, ISOCAM severe field distortion (Okumura 2000) was taken into account as determined by Aussel et al. (1999).

Following this procedure, both unreconstructed and reconstructed sky maps are produced. In both cases, two ancillary maps are also constructed. The sky coverage (or 'NPIX') map contains the number of independent 'images' added together to obtain a pixel value in the final map. On the other hand, the noise (or 'RMS') map contains the estimate of the rms noise of each single pixel in the final map, computed by scaling the rms noise of the map as measured at its centre according to the inverse square root of the sky coverage map.

Source detection is then performed on unreconstructed sky maps. First, all pixels above a conservatively low flux threshold (60 μJy)

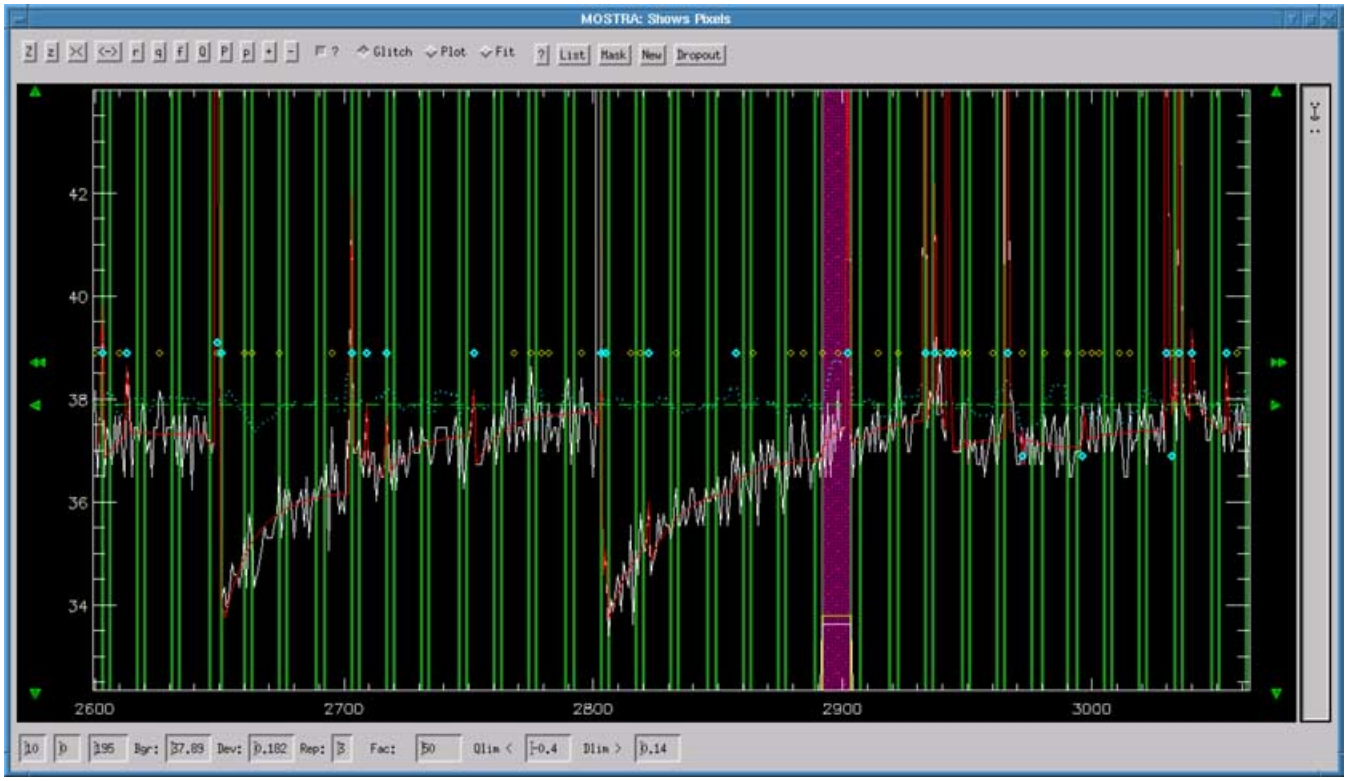

Figure 4. A screenshot of the IDL widget-based graphical user interface used to carry out interactive analysis. The jagged solid (white online) line represents signal, the smooth solid (red online) line modelled signal, the empty (blue online) dots are glitches used in the fitting, the solid (yellow online) dots are readouts flagged as glitches but not used in the fitting, the pairs of vertical (green online) lines flag when the satellite was moving from one pointing to the next one.

are selected, then the IDL Astronomy User's Library `find` routine (an IDL faithful implementation of the homonymous routine of DAOPHOT, particularly suited for the detection of point-like sources in crowded fields) is used to identify positive brightness perturbations around these pixels and return their peak flux, S/N, centroid and shape parameters such as roundness and sharpness.

At this stage, further interactive checks are performed on all sources detected with a S/N ratio greater than 5 to assess their reliability. More specifically, sources detected on the sky map are projected back on to the time history to identify all raster pointings over different pixels where the source is supposed to contribute a significant signal. Then all these pointings are individually checked and, if necessary, refitted, to improve the fit and thus recover lost signals or remove spurious ones. This leads to the visual inspection of all portions of the data where a given $S/N > 5$ source should appear on the basis of its position, and to the discarding of the source altogether if this is found only in a limited number of cases. The overall results of these further checks are an increased reliability and an improved astrometric and photometric accuracy.

3.6 Mosaicing

Up to this stage, all rasters are reduced and processed individually. However, in order to fully exploit the limited redundancy of the observations, a technique to build a mosaic out of rasters covering the same field was devised. This is carried out as follows. Once the reduction of all rasters of interest is completed according to the above procedure, the necessary corrections to nominal astrometry are determined as the median offset between ELAIS source positions expressed with respect to nominal astrometry and the positions of USNO A2.0 sources found in the field. This is done through a two-step process. First, the two catalogues are cross-correlated, assigning to each ELAIS sources its closest United States Naval Observatory (USNO) association. The median of the positional differences thus determined, excluding ELAIS sources with no USNO association within 12 arcsec, is computed and assumed as a first-order correction to ELAIS source positions. The cross-correlation procedure is then repeated to calculate a second-order astrometric correction in exactly the same way, the only difference being that ELAIS sources with no USNO identification within three times the root mean square deviation of the ELAIS–USNO association distance are also excluded during this second step. This leads to the identification of an average of 43 USNO sources in our catalogue. This two-step correction is assumed as the raster offset with respect to nominal astrometry, and the root mean square deviation of ELAIS-USNO distances as the error in the offset determination. Deviations from nominal astrometry have long been known to be significant in *ISO* raster observations, and this is confirmed by our results, which are summarized in Table 3. Most total offsets are greater than or of the order of the pixel field of view size (6 arcsec), their mean value being 7 arcsec, whereas associated errors have a mean value of 0.39 arcsec. The small errors are not only owing to the careful data reduction, but also to the large number of ELAIS sources, and largely contribute to the very good overall astrometric accuracy quantified in Section 7. In addition, our mean offset is consistent with Sato et al. (2003), who found a mean offset of 6 arcsec in five LW2 raster observations.

A common mosaic grid is then built on which different rasters belonging to the same field are projected taking into account astrometric offsets. Mapping, source extraction, projection of sources

Table 3. Astrometric offsets of ELAIS rasters. Corrections to *ISO* nominal astrometry as determined through cross-correlation between ELAIS and USNO A2.0 source lists.

Raster	Nominal position		RA (arcsec)	Dec. (arcsec)	Total (arcsec)
	RA (J2000)	Dec. (J2000)	Offset ± error	Offset ± error	Offset ± error
S1_1	00 30 25.40	−42 57 00.3	−2.06 ± 0.40	−4.46 ± 0.38	4.91 ± 0.55
S1_2	00 31 08.20	−43 36 14.1	−3.24 ± 0.22	+6.86 ± 0.29	7.59 ± 0.36
S1_3	00 31 51.90	−44 15 27.0	+1.57 ± 0.29	−7.75 ± 0.33	7.91 ± 0.44
S1_4	00 33 59.40	−42 49 03.1	+0.23 ± 0.22	−4.01 ± 0.27	4.02 ± 0.35
S1_5_A	00 34 44.40	−43 28 12.0	−3.50 ± 0.23	+9.63 ± 0.27	10.24 ± 0.35
S1_5_B	00 34 44.40	−43 28 12.0	−0.52 ± 0.21	−8.10 ± 0.26	8.12 ± 0.33
S1_5_C	00 34 44.40	−43 28 12.0	−3.04 ± 0.24	+5.34 ± 0.29	6.14 ± 0.38
S1_6	00 35 30.40	−44 07 19.8	+0.60 ± 0.43	−7.14 ± 0.24	7.17 ± 0.49
S1_7	00 37 32.50	−42 40 41.2	+1.26 ± 0.22	−5.62 ± 0.38	5.76 ± 0.44
S1_8	00 38 19.60	−43 19 44.5	+0.72 ± 0.22	−5.31 ± 0.24	5.36 ± 0.36
S1_9	00 39 07.80	−43 58 46.6	−2.34 ± 0.19	+4.61 ± 0.23	5.17 ± 0.30
N1_1	16 15 01.00	+54 20 41.0	+1.96 ± 0.34	−9.34 ± 0.21	9.54 ± 0.40
N1_2_A	16 13 57.10	+54 59 35.9	+3.27 ± 0.31	−9.48 ± 0.22	10.02 ± 0.38
N1_2_B	16 13 57.10	+54 59 35.9	+4.17 ± 0.23	−7.89 ± 0.15	8.92 ± 0.27
N1_3	16 10 34.90	+54 11 12.7	−1.04 ± 0.42	−6.18 ± 0.25	6.27 ± 0.49
N1_4	16 09 27.00	+54 49 58.7	+4.60 ± 0.44	−6.71 ± 0.23	8.14 ± 0.50
N1_5	16 06 10.80	+54 01 08.0	−8.90 ± 0.27	+3.77 ± 0.18	9.67 ± 0.32
N1_6	16 04 59.00	+54 39 44.3	−8.71 ± 0.32	+3.88 ± 0.22	9.54 ± 0.39
N2_1	16 32 59.80	+41 13 33.2	−4.68 ± 0.23	+7.18 ± 0.21	8.57 ± 0.31
N2_2	16 34 44.50	+40 38 45.0	+2.93 ± 0.27	−2.87 ± 0.274	4.10 ± 0.38
N2_3	16 36 05.50	+41 33 11.8	−5.50 ± 0.46	+7.30 ± 0.37	9.14 ± 0.59
N2_4	16 37 48.90	+40 58 13.1	−5.36 ± 0.24	+7.46 ± 0.21	9.19 ± 0.32
N2_5	16 39 13.80	+41 52 31.6	−5.43 ± 0.29	+7.32 ± 0.24	9.11 ± 0.38
N2_6	16 40 55.50	+41 17 22.7	−2.45 ± 0.28	+2.32 ± 0.24	3.38 ± 0.37
N2_R_A	16 35 45.00	+41 06 00.0	+1.29 ± 0.33	+6.01 ± 0.21	6.15 ± 0.39
N2_R_B	16 35 45.00	+41 06 00.0	+5.91 ± 0.34	+4.24 ± 0.22	7.27 ± 0.40
N3_3	14 29 38.30	+33 24 49.6	−1.39 ± 0.30	−3.44 ± 0.16	3.71 ± 0.34
N3_5	14 32 38.20	+33 11 10.3	−0.17 ± 0.31	−3.52 ± 0.24	3.52 ± 0.39

detected with a S/N ratio greater than 5 back on time history and interactive checks are further performed on this mosaic sky map exactly as on single raster sky maps. The quality of data reduction is thus improved through cross-checks of sources detected on different rasters, increasing reliability and completeness in repeatedly observed regions and partly overcoming the otherwise severe problems at raster boundaries. The final S/N ratio sky maps of the four fields are shown in Figs 5, 6, 7 and 8. Typical noise levels are between 20 and 30 μJy^{-1} pixel. Such maps, together with noise and sky coverage maps, are available at `http://astro.imperial.ac.uk/~vaccari/elais`.

4 AUTOSIMULATION

Even after a very careful reduction, flux determination is a very delicate process owing to the interplay of different factors, the most important being mapping effects related to PSF undersampling, the transients of the detector and other trends owing to the limits of the adopted reduction method. Mapping effects are particularly tricky, as they determine the way one obtain source total fluxes from corresponding peak fluxes measured on sky maps by source detection software. Clearly, the conversion factor between these two quantities is very much dependent on the source position, specifically on its relative position with respect to the centre of the sky map pixel. Namely, if a source falls near the boundary between two or more pixels, its total flux will be spread between these pixels and thus peak flux will be much smaller than total flux. Conversely, if a source falls right at the centre of a pixel a greater percentage of its total flux will be contained in this pixel, and thus peak flux will be nearer to total flux. The technique we developed, which we called **autosimulation**, was conceived to model and insofar as possible take into account mapping and data-reduction effects on flux determination by first constructing both real and theoretical (i.e. noise-free) sky maps, and then use the latter ones to correct fluxes obtained from the former ones. Autosimulation consists in simulating sources, on top of noise-free maps, at each position where a source was actually detected (or, for simulations described in Section 5, at their randomly generated positions), calculating the ratio between peak and total flux for the simulated source on such theoretical sky maps, and converting the measured peak flux of the real source to its total flux using such a ratio. Source simulation is carried out in a straightforward way using the same mathematical model the Lari Method is based on, thus also allowing to verify its predictions. In so doing, PSF modelling followed the prescriptions given by Okumura (1998) for stellar PSFs but adopting a spectrum of the form $f_\nu =$ constant, i.e. a closer match to the expected galaxy spectrum than the Rayleigh–Jeans form used for stellar spectra. The resulting PSF is larger than the one computed for stars.

To describe how autosimulation works in some greater detail, a few definitions and relations which will also be useful to discuss the results of simulations described in Section 5 must be summarized as follows.

(i) f_s is the measured peak flux obtained from real (i.e. containing glitches, noise and transients) sky maps. Its value therefore depends on mapping effects, transients and the adopted data-reduction method;

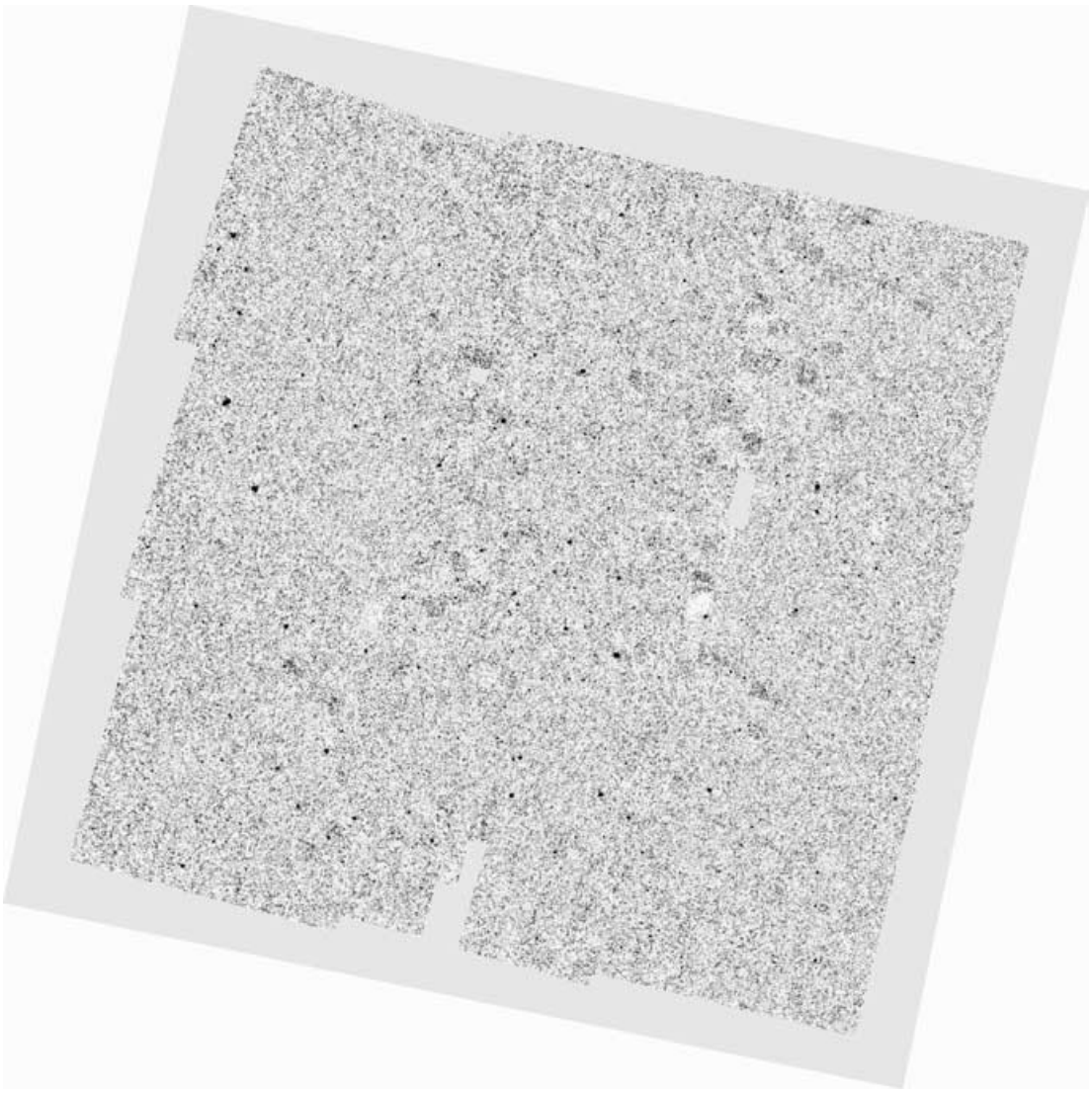

Figure 5. S1 field S/N ratio sky map. Image size is $2.335 \times 2.335\,\mathrm{deg}^2$. North is up and east is left.

(ii) f_0 is the 'theoretical' peak flux obtained from simulated (i.e. containing neither glitches nor noise but taking into account source transients) maps. Its value depends on mapping effects and transients only.

(iii) f_{sr} and f_{0r} are analogous to f_s and f_0 but are built from reconstructed maps, thus recovering the effects of transients. However, as already mentioned and will be later discussed in greater detail, the ability of our software to correctly reconstruct measured fluxes breaks down at faint levels.

The correction factor for mapping effects is computed as follows. A simulated source is generated on each position where a real source was actually detected, assuming a total flux $S_0 = f_s/\langle f_s/S\rangle_{\mathrm{sim}}$ based on the measured peak flux f_s and on the median peak flux/total flux ratio $\langle f_s/S\rangle_{\mathrm{sim}} = 0.216$ obtained from simulations (see Section 5 and Fig. 13). Then the flux estimate corrected for mapping effects is computed as $S = (f_s/f_0)\,S_0$. The same procedure is also carried out for reconstructed fluxes, providing a parallel flux estimate $S_r = (f_{sr}/f_{0r})\,S_{0r}$ which will be compared to the one obtained from unreconstructed fluxes in Section 5.1. Source simulation is carried out using the same model for the charge release adopted in fitting the data. In so doing, however, autosimulation does not correct for more subtle and elusive effects arising from data reduction, which can only be assessed through simulations. This is described in Section 5.1.

Such a procedure provides reliable flux estimates which are well compatible with estimates obtained through conventional aperture photometry for most sources, but is clearly non-optimal when dealing with extended sources. For these, as well as for a few very close or blended sources, aperture photometry usually provide a better estimate of the source flux. After correcting fluxes for mapping effects, potentially extended sources are therefore identified through both visual inspection of sky maps and the calculation of parameters connected to source extension. Sources flagged by these criteria (totalling 67 out of 1923 making up the catalogue, or 3.5 per cent) were then individually treated, aperture photometry with a suitable aperture radius was carried out and the result was adopted as their most reliable flux estimate. As to the overall performance of the autosimulation process when compared with aperture photometry, autosimulated fluxes and their counterparts calculated through aperture photometry are compared for all sources in Section 5.3.

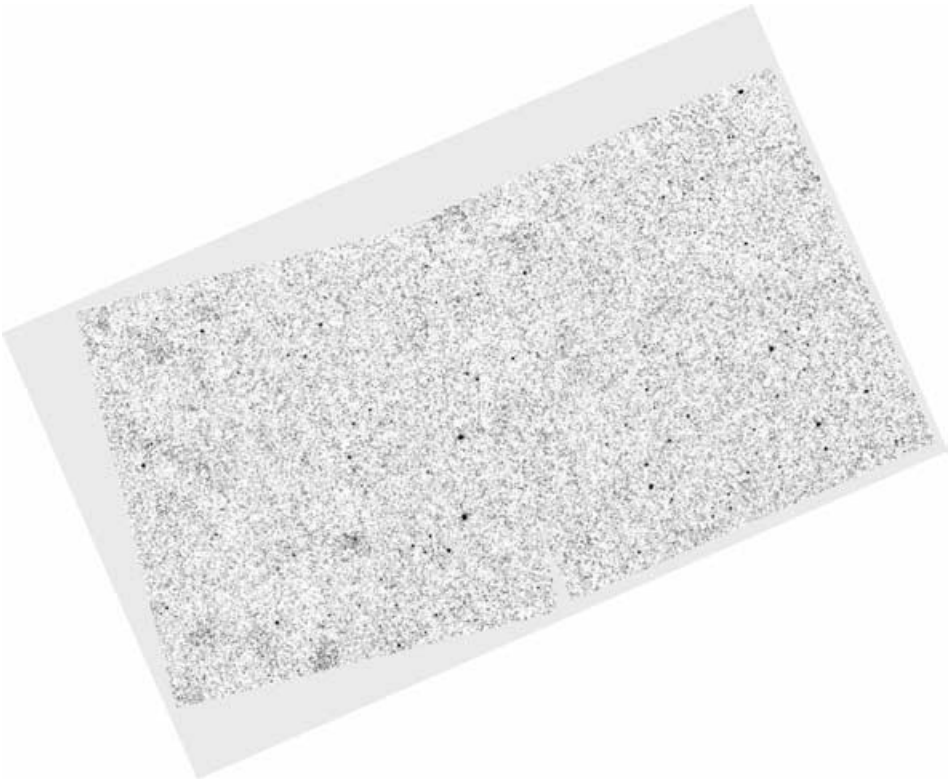

Figure 6. N3 field S/N ratio sky map. Image size is $0.866 \times 1.454\,\mathrm{deg}^2$. North is up and east is left.

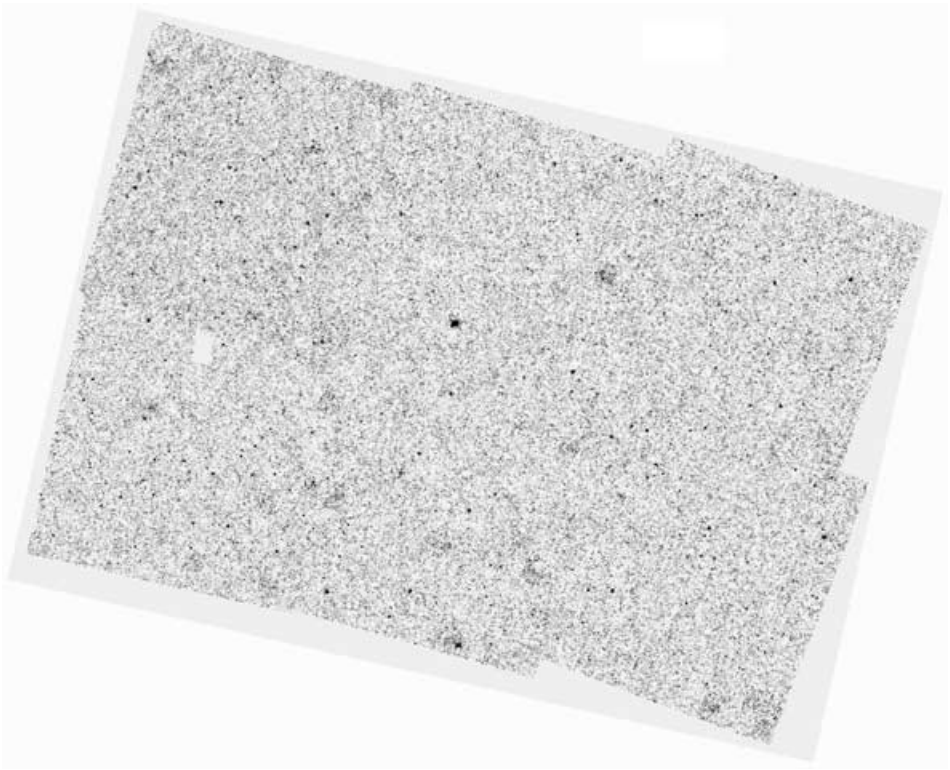

Figure 7. N1 field S/N ratio sky map. Image size is $1.514 \times 2.134\,\mathrm{deg}^2$. North is up and east is left.

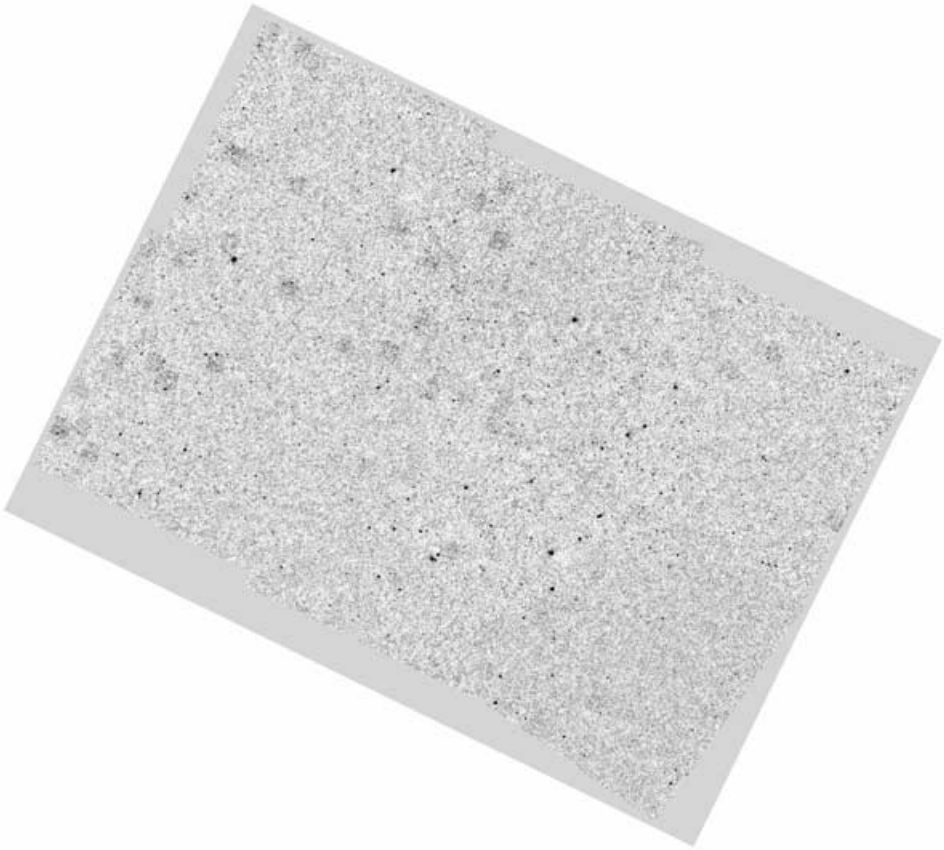

Figure 8. N2 field S/N ratio sky map. Image size is $1.559 \times 2.117\,\mathrm{deg}^2$. North is up and east is left.

5 SIMULATIONS

Owing to the peculiar nature of *ISO* data and of the reduction method employed, it is important to carefully test the performance of the latter on 'ideal' data and sources. In particular, systematic effects on flux estimates related to the data-reduction method can only be probed by these means. Owing to the strong peculiarities of our data set, which is characterized by several noise features on different time-scales, only real data can effectively be taken as representative of instrumental behaviour. Therefore, the effects of artificial sources must be somehow simulated on the top of real pixel time histories, and data reduction must then be carried out exactly as done for real sources. Source confusion in the field is thus slightly increased, but this effect is not critical for ELAIS data. The Lari Method is based on a physical model of the behaviour of the detector, and can therefore make predictions of the effects on the detector of the additional photons from simulated sources in a straightforward way. On this basis, an extensive set of simulations was carried out to assess the effects on flux estimates and the overall performance of data reduction in a statistically meaningful way. The S1 field was chosen for this purpose as the most representative, being the largest and including both regions observed only once and repeatedly observed regions (hereafter, **non-repeated** and **repeated** regions, respectively), therefore allowing one to assess the differences in performance warranted by higher redundancy.

Simulations were carried out as follows. First a set of $N = 600$ random sky positions (excluding regions near to real sources, mosaic sky map boundaries and masked regions of the mosaic sky map, i.e. preventing simulated sources to appear nearer than 15 arcsec to any of these regions) was generated. Then a logarithmically uniform flux distribution covering the range between a lower limit $S_\mathrm{l} = 0.5$ mJy and an upper limit $S_\mathrm{u} = 4.0$ mJy

$$S_n = S_\mathrm{l} \left(\frac{S_\mathrm{u}}{S_\mathrm{l}} \right)^{n/N} \quad \text{for } n = 0, N-1 \tag{5}$$

was coupled with the random positions above to characterize the set of simulated sources. Following the same procedure, 100 more sources were simulated (adopting a flux distribution following the same analytical formula but covering the 0.35–3.5 mJy flux range) in the repeated regions of the field, thus increasing the otherwise low number of simulated sources in these regions. All 700 sources were then projected from their sky position back on to the pixel time history, simulating their effects as superposed on glitches and noise characterizing the real data. In so doing, all portions of time history where simulated sources were predicted to give a sizeable additional signal were identified. The fitting procedure was thus re-run on these regions only, and all steps of data-reduction and flux determination were then carried out on simulated sources exactly as described in Section 3 for real sources. At this stage the positions and fluxes of simulated sources that had been detected with a S/N ratio greater than 5 were compared with the input values to calibrate and evaluate the performance provided by our data-reduction method in different respects. The overall number of simulated and detected sources is given in Table 4, whereas the following sections detail all relevant aspects of simulations, apart from the completeness estimates which will be described by Lari et al. (in preparation) in order to obtain extragalactic source counts.

Table 4. Number of simulated and detected sources. Total figures are given together with those for non-repeated and repeated regions.

	Non-repeated	Repeated	Total
Simulated sources	502	198	700
Detected sources	230	125	355

5.1 Flux determination

The autosimulation process we use for flux determination, though relatively simple in principle, leads to several systematic effects which need to be carefully taken into account in order to understand how it can provide us with the best estimate of source fluxes. The analysis of its results on simulated sources will also allow us to test the goodness of our model and the reliability of the related signal reconstruction process. As described in Section 4, autosimulation involves simulating theoretical (i.e. noise-free) maps containing all (i.e. both real and simulated) sources of interest, then carrying out signal reconstruction on both theoretical and real sky maps, thus determining the theoretical ratio between peak and total fluxes, and finally applying results determined on theoretical maps to correct real fluxes.

Fig. 9 shows how mapping effects affect the relation between peak fluxes and total fluxes for both reconstructed and unreconstructed theoretical sky maps. Following the nomenclature adopted in Section 4, the histogram distribution of f_0/S_0 and f_{0r}/S_0 ratios are plotted for all sources (top panel) and separately for non-repeated and repeated regions (bottom panel). While the two distributions for non-repeated and repeated regions peak at slightly different values and thus have a (marginally) smaller width, the f_{0r}/f_0 ratio is remarkably similar, 1.61 being its mean value. This means that, according to our model, owing to the short integration time adopted in observations with respect to the time constant of the response of the detector, the measured flux, even in a noise-free image, will only equal 60 per cent of the incident flux.

In order to correctly determine fluxes, however, one needs to make use of the modelling of the detector employed and thus compare real fluxes with theoretical ones. By means of the f_s/f_0 histogram distribution, Fig. 10 shows how real peak fluxes are systematically lower than theoretical ones, owing to limits of the data-reduction method and to the presence of noise. The width of the f_s/f_0 distribution is quite large, peaking at 0.83, showing a predictable narrowing of the distribution at bright fluxes but on the whole a negligible dependence on flux (Fig. 10, top panel, see also Fig. 11). Conversely, values for non-repeated and repeated regions differ in a measurable way, mean values being 0.81 and 0.87, respectively (Fig. 10, bottom panel). The rms half-widths of the distributions are 0.17 and 0.12 in the two cases, respectively, which also provides an estimate of the photometric error in different regions, which is smaller in the repeated regions, as it was to be expected. While photometric error will be assessed by different means in Section 8, this already indicates how repeated observations allow, through interactive analysis,

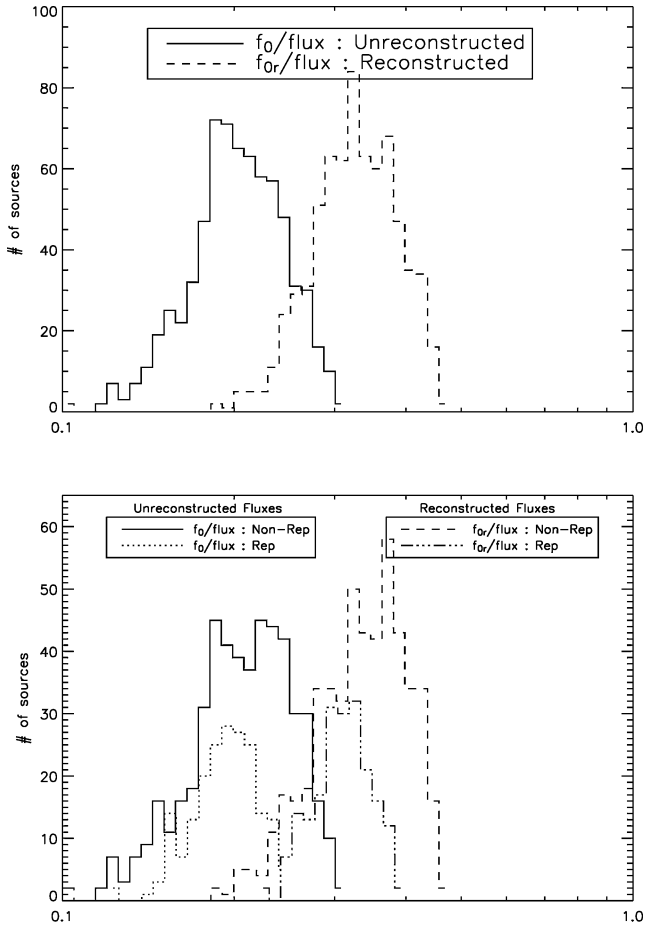

Figure 9. Peak/total flux ratio for theoretical sky maps. Histogram distribution for both unreconstructed and reconstructed maps are given. Overall distributions are shown (top panel) together with those for non-repeated and repeated regions separately (bottom panel).

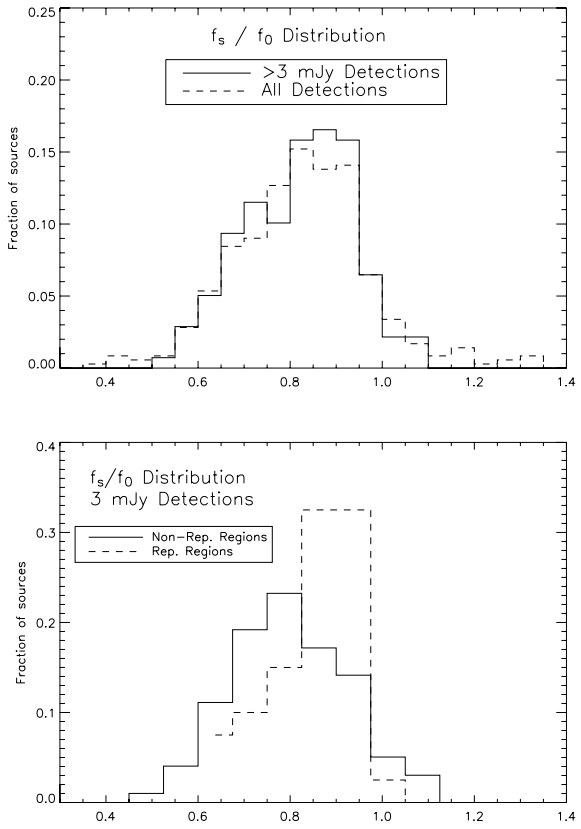

Figure 10. Real/theoretical peak flux ratio distribution. The comparison between distributions for all detections and for bright source (>3 mJy) detections is shown (top panel) together with the same comparison for detections in non-repeated and repeated regions (bottom panel).

a better and more robust recovery of the source total flux, leading to a smaller flux correction (i.e. an higher f_s/f_0 ratio) and a smaller dispersion.

Fig. 11 confirms the moderately small spread of the f_s/f_0 distribution and also shows the good linearity displayed by the f_s versus f_0 relation, as long as a source is detected. Provided a suitable flux correction is applied to account for the f_s/f_0 distribution (see Section 5.2), this allows to confidently use our results at all the catalogue flux levels.

Fig. 12 shows how well the signal reconstruction process carried out by the fitting procedure works at different fluxes. At can be clearly seen, below a certain flux, f_s/f_{sr} systematically falls below f_0/f_{0r}, that is, the goodness of signal reconstruction breaks down at the faint end. It was thus decided to use only unreconstructed fluxes in flux determination, so as to provide a flux estimate that would be reliable at all flux levels. Therefore, when not explicitly mentioned, hereafter we will refer to unreconstructed signal and fluxes only.

Finally, and most importantly, Fig. 13 shows how total injected fluxes and peak real fluxes are related to each other. The relation mimics the one between f_s and f_0 already shown in Fig. 11, a linear relation with a reasonably small spread (the mean value of the S/f_s ratio being 4.64), warranting a reliable determination of total fluxes on the basis of measured peak fluxes.

5.2 Flux correction

Systematic effects on flux estimates described in previous Section were modelled and taken into account using results from simulations and following Gruppioni et al. (2002). According to this approach, the correction to be applied to flux estimates obtained through autosimulation is derived from the the so-called g function, which describes the S/N-dependent distribution of the f_s/f_0 ratio. The g function is obtained as the combination of the intrinsic (i.e. high-S/N) g function, or g_0 function, and a term owing to noise. First, the g_0 function is derived from the distribution of the f_s/f_0 ratio obtained for bright ($S > 3$ mJy) simulated sources (see Fig. 10), by modelling and correcting for the small degree of incompleteness to be expected at such fluxes. Then convolution with a variable noise term is carried out to obtain the overall S/N-dependent g function. Finally, for each S/N value, the median f_s/f_0 ratio for detectable (i.e. $f_s > 5\sigma$) sources, or $q_{\rm med}$, is computed. Autosimulated fluxes

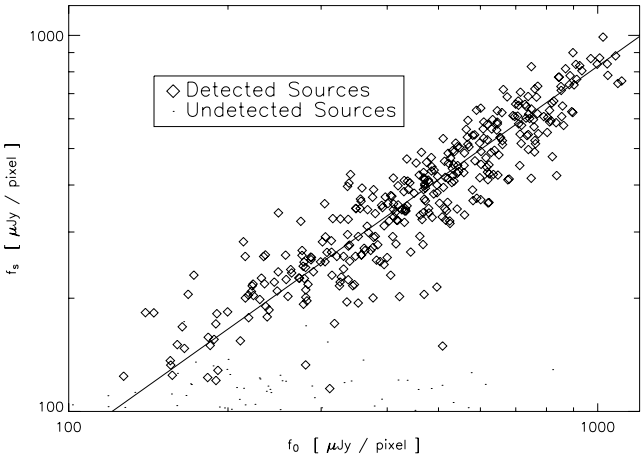

Figure 11. Real versus theoretical peak flux. The $f_s = 0.83\ f_0$ line, corresponding to the 0.83 mean value of the f_s/f_0 ratio for detected sources, is also plotted.

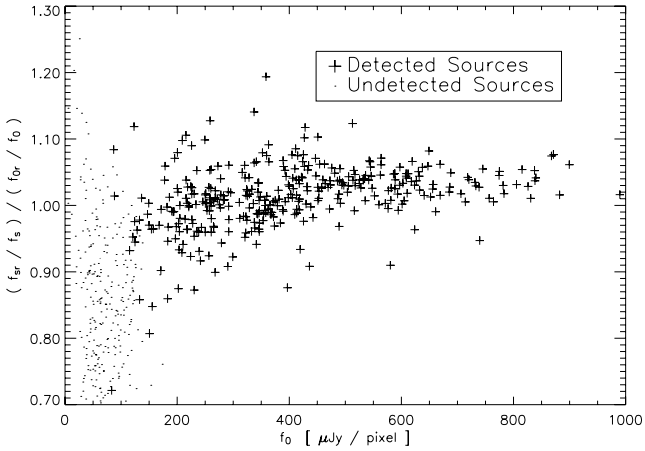

Figure 12. Signal reconstruction as function of real peak flux.

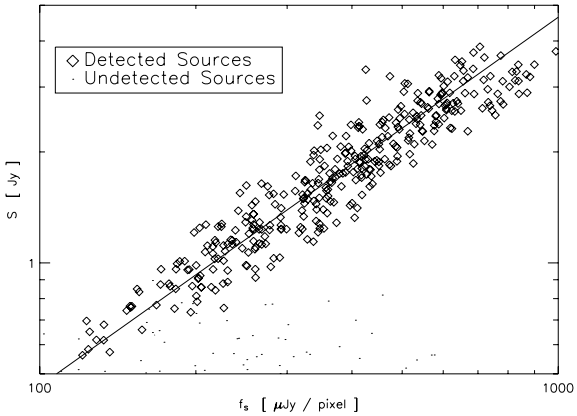

Figure 13. Total versus peak flux. The $S = 4.64\ f_s$ line, corresponding to the 4.64 mean value of the S/f_s ratio for detected sources, is also plotted.

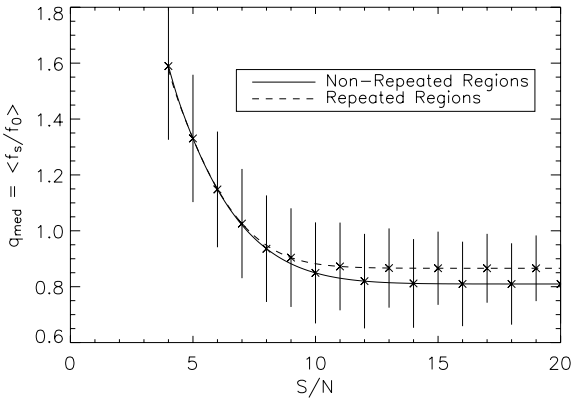

Figure 14. Flux correction applied to autosimulated fluxes. The inverse of the correction factor, or $q_{\rm med}$, is plotted against S/N ratio for non-repeated and repeated regions. Error bars attached to the two curves indicate the dispersion of such flux correction.

are then corrected by a factor $1/q_{\rm med}$. The dispersion of this curve is also calculated, providing an ideal lower limit to the photometric accuracy achievable with this method. This process was carried out separately for non-repeated and repeated regions, and the results are plotted in Fig. 14. The two $q_{\rm med}$ curves asymptotically tend to the average f_s/f_0 values 0.81 and 0.87 determined for simulated

sources in non-repeated and repeated regions, while they virtually coincide and then soar below the S/N $\sim$ 7 level, where noise starts to dominate over the effects of redundancy and $q_{\rm med} \sim 1$. At bright fluxes, the dispersion of the two curves asymptotically tend to 0.12 and 0.09 for non-repeated and repeated regions.

It must be emphasized how all of the above applies to 'relative' fluxes determined with respect to *ISO* LW3 standard sensitivity. In Section 9 the absolute flux calibration of our catalogue will be discussed on the basis of the comparison between measured and predicted mid-infrared stellar fluxes and with respect to *IRAS* standard calibration.

5.3 Autosimulation versus aperture photometry

The performance of the autosimulation technique for flux determination described in Section 4 can also be assessed comparing the total fluxes obtained with this procedure with those obtained by means of ordinary aperture photometry.

The relation between these two quantities shows good linearity for most sources, as it is shown for simulated sources in Fig. 15. Plotted aperture fluxes were computed adopting an aperture of 6-arcsec radius and correcting both for the transients and for the 40 per cent of the instrumental PSF falling beyond this aperture. Such an aperture was chosen as the most reliable trade-off allowing one to reliably include most of the source flux and least of the background.

Only a few sources depart substantially from the 1:1 relation, with 94 per cent of sources with fluxes in accordance within 20 per cent and an overall rms deviation of 12 per cent. On the whole, our flux determination procedure is therefore consistent with conventional aperture photometry, provided a proper correction for PSF effects is applied.

5.4 Catalogue flux distribution

Flux distribution of catalogue sources is illustrated in Fig. 16, with 50 per cent of the sources having fluxes greater than 1.65 mJy, 76 per cent greater than 1.2 mJy and 89 per cent greater than 1 mJy. As it can be clearly seen from the two separately plotted histograms, sources in non-repeated regions largely prevail in number down to about 1.5 mJy, at which flux their number per flux bin drops sharply. Conversely, the number of sources per flux bin in repeated regions continue to increase, albeit slowly, down to 1 mJy, where they already amount to about 50 per cent of the total (i.e. detected in both repeated and non-repeated regions in a given flux bin) number of sources, compared to about 15 per cent of the total observed area. While detailed completeness estimates will be described by Lari et al. (in preparation), this plot already indicates how the catalogue is largely complete up to $\sim$1.5 mJy, and slightly fainter than that in repeated regions.

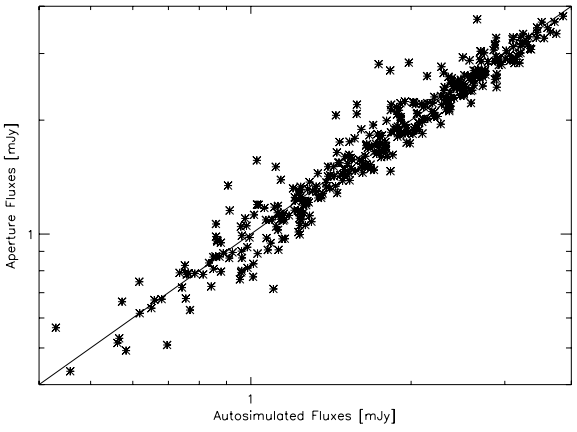

Figure 15. Autosimulated total fluxes versus aperture fluxes.

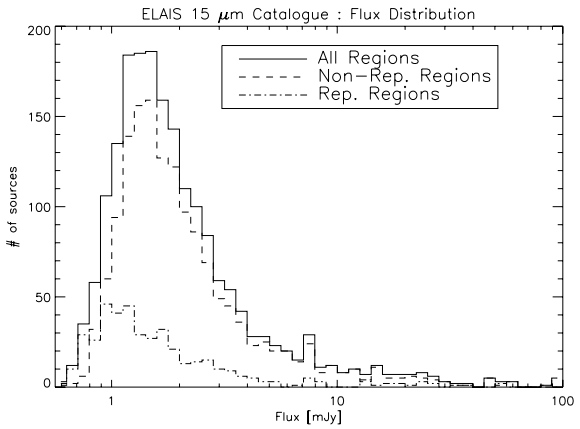

Figure 16. Histogram flux distribution of ELAIS sources. All regions, non-repeated and repeated regions are plotted.

6 OPTICAL IDENTIFICATIONS

Identification of 15-μm sources was carried out on both archival and deep imaging obtained for this purpose at optical and near-infrared wavelengths. This provided optimal stellar discrimination as well as optical and near-infrared flux measurements over the whole large flux range probed by our catalogue, thus ultimately leading to a very reliable 15-μm photometric calibration (see Section 9).

The S1 field was surveyed in R down to $R \sim 23.0$ by La Franca et al. (2005) using the 1.5-m Danish/ESO telescope, and the identification of the 462 15-μm sources from Lari et al. (2001) was extended to the newly detected sources. The N1 and N2 fields were surveyed in U, g', r', i' and Z down to 23.4, 24.9, 24.0, 23.2 and 21.9, respectively, as part of the Wide Field Survey (McMahon et al. 2001), using the Wide Field Camera at the Isaac Newton Telescope. Identifications of N1 and N2 15-μm sources were obtained by Gonzalez-Solares et al. (2005) using a maximum likelihood method with an 0.7 likelihood threshold. Deep near-infrared imaging of areas around selected 15-μm sources in N1 and N2 was carried out by Väisänen et al. (2002). No original imaging material was available in the N3 field. Furthermore, the USNO A2.0, Guide Star Catalog 2.2, Tycho-2, Two Micron All Sky Survey (2MASS) All-Sky Data Release and APM catalogues were cross-correlated with 15-μm sources so as to provide a list of tentative identifications. 15-μm contours were superimposed on Digitized Sky Survey and 2MASS images as well as on to new observational material, yielding diagnostic finding charts for extended, blended and disturbed sources.

Generally speaking, the identification based on deep optical imaging and automated source extraction and classification carried out with SEXTRACTOR was usually chosen, but archival material proved essential in dealing with bright sources, which appeared as being saturated in deep observations, and in providing measurements for sources in the N3 or in small portions of the other three fields, where deep optical imaging had not been obtained. In particular, a positional difference of 6 arcsec, corresponding to three times the maximum estimated astrometric error of the 15-μm data-reduction

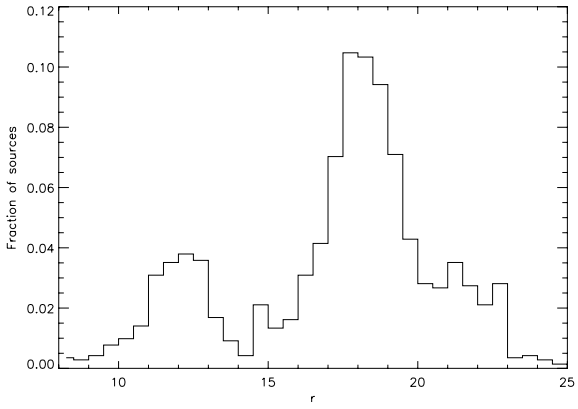

Figure 17. Magnitude distribution of optical IDs of 15-μm sources. The two peaks at $r \sim 12$ and $r \sim 18$ are associated with stellar and extragalactic IDs, respectively.

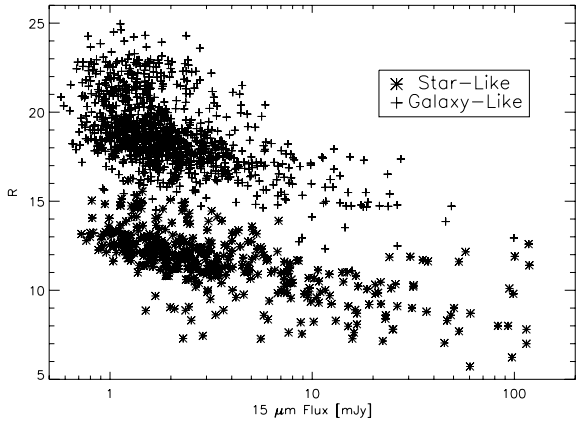

Figure 18. 15-μm versus *R* flux–flux diagram of identified sources. Stellar and extragalactic IDs are indicated.

Table 5. Some basic properties of the catalogue divided into different fields.

Field	Area	Sources	Stars		IDs	
	(deg^2)	No.	No.	per cent	No.	per cent
S1	4.17	736	145	19.7	584	79.3
N1	2.84	490	121	24.7	441	90.0
N2	2.84	566	126	22.3	493	87.1
N3	1.00	131	29	22.1	103	78.6
Total	10.85	1923	421	21.9	1621	84.3

process (see Section 6), was adopted as a cut-off ensuring a safe identification.

The magnitude distribution of the sources identified as optical counterparts of 15-μm sources through this process is plotted in histogram form in Fig. 17, showing a bimodal distribution whose two peaks are to be associated with stars and galaxies and sharply cutting-off at $R \sim 23$. The number of stars and total sources identified according to this criterion, is separately reported for the four fields in Table 5. About 90 per cent of 15-μm sources are assigned a robust optical association in N1 and N2 fields, while owing to the shallower depth this fraction drops to about 80 per cent in the S1 and N3 fields. The average fraction of identified sources amount to 84.3 per cent. Conversely, the statistics of stellar identifications is remarkably uniform between the four fields, with a 22 per cent of stars and small field-to-field differences.

Figs 18 and 19 show how, at least down to the 15-μm flux limit probed by ELAIS, it is further possible to effectively discriminate between stars and galaxies solely on the basis of the comparison between optical and near-infrared magnitudes with 15-μm fluxes, thus demonstrating the robustness of the identification process.

7 ASTROMETRIC ACCURACY

The optical identification process also allowed us to assess the astrometric accuracy achieved in 15-μm data reduction independently of simulations. In our case, astrometric errors can be considered as the combination of three error sources associated with the detector spatial sampling σ_s, the reduction method σ_r and the instrumental pointing accuracy σ_p, respectively.

The combination of the σ_s and σ_r terms, which we will hereafter indicate as σ_{s+r}, can be evaluated from simulations, comparing the injected positions of simulated sources with the corresponding detected positions, whereas the σ_p term is given by the error on the

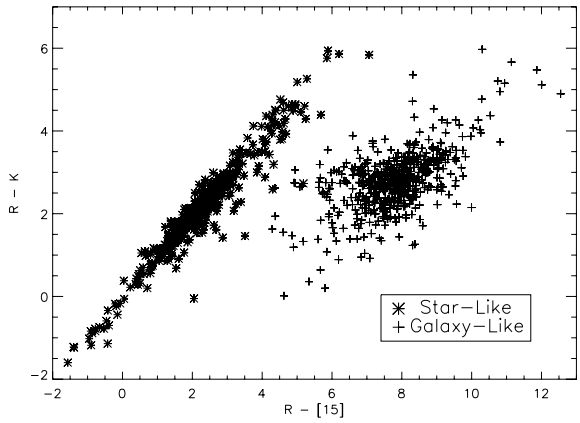

Figure 19. $R - K$ versus $R - [15]$ colour–colour diagram of identified sources. Stellar and extragalactic IDs are indicated. The [15] magnitude scale is defined in equation (9).

astrometric offset of the rasters, as derived in Section 3.6. The total astrometric error will then be given by

$$\sigma_{tot} = \sqrt{\sigma_{s+r}^2 + \sigma_p^2}. \quad (6)$$

The overall distribution of the differences between injected and detected positions of simulated sources is shown in histogram form in Fig. 20 for both non-repeated and repeated regions. Differences in RA and Dec. are distributed in a remarkably similar way, which will allow us to use them together in the following statistical analysis, so as to increase our sample. About 75 per cent simulated sources are detected within 1 arcsec of their injected positions and about 96 per cent within 2 arcsec. Dependence of σ_{s+r} on S/N ratio can be evaluated binning simulated sources according to their S/N ratio and computing the median positional difference of each bin. Thus one obtains the σ_{s+r} term as function of S/N. The σ_p term is obtained as the median value of astrometric offset errors per component reported in Table 3, that is 0.39 arcsec per component irrespectively of S/N. The total astrometric error per component is then computed through equation (6). The results are illustrated in Fig. 21, showing total astrometric errors for sources detected both in non-repeated and repeated regions as a function of S/N ratio for S/N < 30. The astrometric accuracy turns out to be very good, with errors being as low as 0.7 and 0.8 arcsec per component at the bright end in non-repeated and repeated regions, respectively.

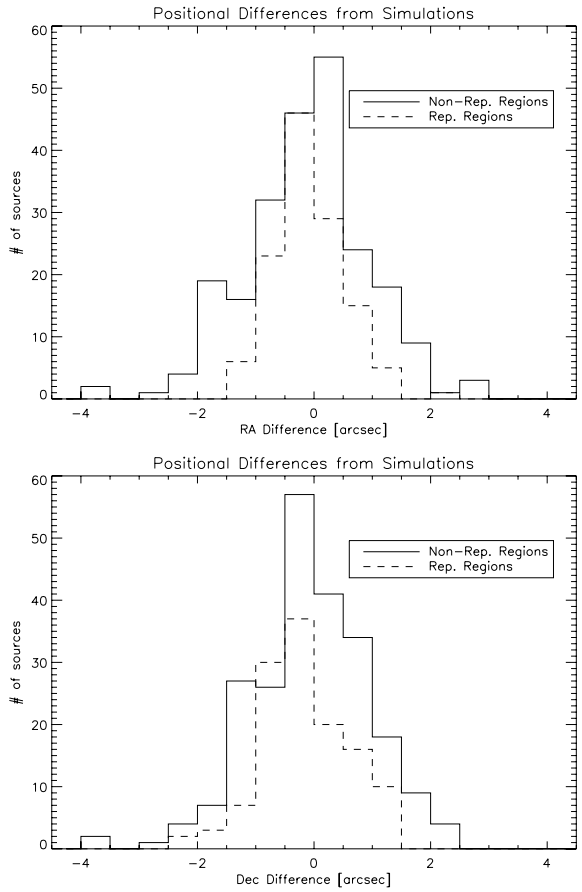

Figure 20. Sampling and reduction astrometric error. Positional differences between injected and detected simulated sources in RA and Dec.

Catalogue astrometric errors can be estimated by fitting polynomials to the $\log \sigma_{\rm tot}$ versus $\log S/N$ curves for non-repeated and repeated regions derived from simulations. At the faint end, however, the errors computed in repeated regions unrealistically flatten below S/N $\sim$ 10, owing to the poor statistics following from the low number of simulated sources that are detected at low S/N ratio levels. For this reason, we cross-checked the astrometric accuracy evaluated from simulations against an independent estimate based on optical identifications of catalogue sources (see Section 6). The same binning process described above was carried out on positional differences between catalogue sources and their optical counterparts, yielding the results plotted in Fig. 21. The thus-derived $\sigma_{\rm tot}$ versus S/N ratio relation closely follows a straight line in the log–log plane at $5 < S/N < 20$, and closely resembles the one derived from simulations at $10 < S/N < 20$, confirming the overall robustness of the simulation process. It was thus decided to estimate catalogue astrometric errors by fitting a straight line to the $\log \sigma_{\rm tot}$ versus $\log S/N$ curves for non-repeated and repeated regions derived from optical identifications. At S/N $>$ 20, other effects such as the widening of the instrumental PSF and the increase of the optical astrometric error begin dominating the astrometric error budget, and the astrometric error curve starts showing irregularities, so that linear fitting cannot be reliably assumed to describe the actual astrometric error. Accordingly, values obtained from simple extrapolation of the straight line obtained at S/N $<$ 20 to higher S/N ratio were truncated when they were deemed too optimistic, i.e. at the 0.8- and 0.7-arcsec values for non-repeated and repeated regions, corresponding to the extrapolated values for S/N $\sim$ 25.

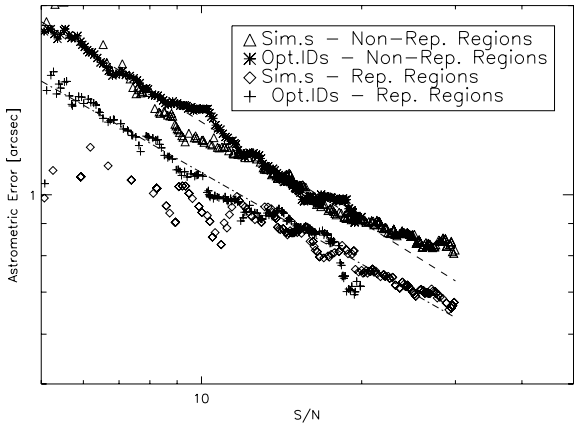

Figure 21. Astrometric accuracy. Total astrometric errors per component as function of S/N ratio in non-repeated and repeated regions. Median positional differences over S/N ratio bins are given. Polynomial fitting curves used for the evaluation of the catalogue astrometric error are also indicated.

8 PHOTOMETRIC ACCURACY

Errors in flux determination using our method can mainly be attributed to two effects, namely the autosimulation process and the noise present on the sky maps. The first contribution can be estimated by computing the width of the $f_{\rm s}/f_0$ distribution shown in Fig. 10 for high S/N ratio sources only, so as to evaluate the effects of the autosimulation process on relatively noise-free maps. At lower S/N ratios, photometric errors arising from noise on the sky maps will combine with those arising from autosimulation. The overall error is thus given by

$$\left(\frac{\Delta S}{S}\right)^2 = \Delta\left(\frac{f_{\rm s}}{f_0}\right)^2 + \left(\frac{\sigma_{\rm map}}{f_{\rm s}}\right)^2 = \Delta\left(\frac{f_{\rm s}}{f_0}\right)^2 + \left(\frac{1}{S/N}\right)^2 \quad (7)$$

where $\Delta(f_{\rm s}/f_0)$ is the width of the $f_{\rm s}/f_0$ distribution as measured for high S/N ratio sources for non-repeated regions and repeated regions separately, and $\sigma_{\rm map}$ is the noise as measured at each source position on the sky map. The first term is a constant, about 0.15 and 0.11 for non-repeated and repeated regions, respectively. This term dominates the photometric error budget at a high S/N ratio, whereas the importance of the second term increases when the S/N ratio decreases. Photometric errors estimated using equation (7) are shown in Fig. 22. The values for S/N $\sim$ 10 are 0.18/0.15 for non-repeated/repeated regions, while they increase to 0.25/0.23 for S/N $\sim$ 5.

9 PHOTOMETRIC CALIBRATION

The standard sensitivity of the *ISO* LW3 channel is of 1.96 ADU/Gain/s/mJy, which can be used to calibrate our catalogue fluxes. However, given the large sample at our disposal, the accuracy of such photometric calibration can be tested against the independently determined *IRAS* standard photometric calibration by studying detected sources with stellar counterparts. Aussel (in preparation) performed a detailed study of mid-infrared emission from stars, using large samples drawn from the *IRAS* Faint Source Catalogue with counterparts in the 2MASS and Tycho-2 (Høg et al. 2000) catalogues. In the two cases, it is found that the $J - K$ and $B - V$ colours of stars are extremely well correlated with the $K -$ [12] and $B -$ [12] colours, respectively, where [12] is a magnitude scale constructed from the *IRAS* 12-μm flux, following the prescriptions of Omont et al. (1999). This relation allows one to accurately

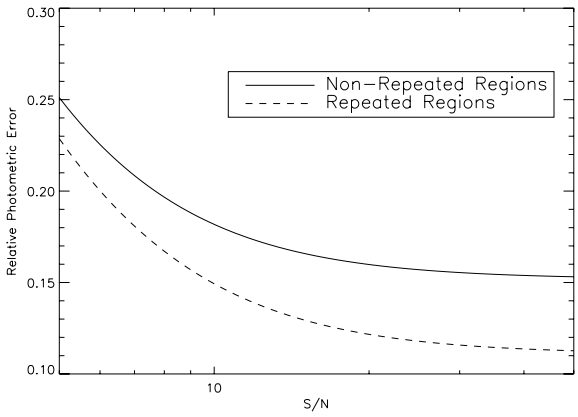

Figure 22. Relative photometric error as function of S/N ratio as given by equation (7) for non-repeated and repeated regions.

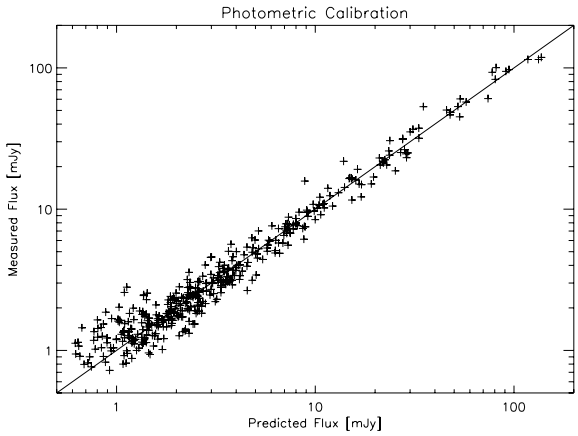

Figure 23. Photometric calibration. Measured versus predicted 15-μm stellar fluxes. The 1.0974 correction factor to measured fluxes is here already taken into account, and the one-to-one relation is also plotted.

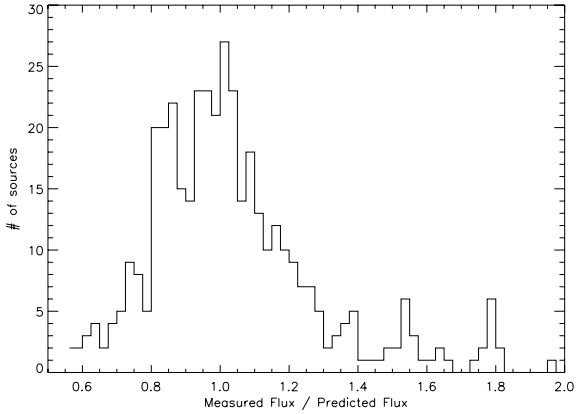

Figure 24. Photometric calibration. Histogram distribution of measured/predicted 15-μm stellar flux ratio. The 1.0974 correction factor to measured fluxes is here already taken into account.

predict the *IRAS* 12-μm flux of a star, provided that its J and K (or B and V) are known and that $J - K$ (or $B - V$) are within certain limits. Stellar atmosphere models (Lejeune, Cuisinier & Buser 1998) show that such colour criteria select stellar spectral types for which the ratio between the 15-μm and the 12-μm fluxes is essentially constant. Thus, if one has access to a substantial number of optical and/or near-infrared counterparts to 15-μm sources, it is possible to use the correlations by Aussel (in preparation) to predict the 15-μm fluxes of *ISO*-detected stars and compare them to the measured values. Such a comparison then allows to investigate possible systematic differences between the two sets of fluxes, which should be attributable to discrepancies between the independently established *IRAS* and *ISO* calibrations. Given the tighter nature of the near-infrared/mid-infrared correlation over a wide range of fluxes with respect to the optical/mid-infrared one, it was decided to use the former, that is expressed by

$$K - [15] = 0.044 + 0.098\,(J - K), \tag{8}$$

where [15] is a magnitude scale defined as

$$[15] = 3.202 - 2.5\log\,(S_{15\ \mu\mathrm{m}}[\mathrm{mJy}]), \tag{9}$$

to compute the predicted fluxes. 2MASS All-Sky Release fluxes were used for the majority of the sources together with fluxes determined for fainter sources as part of the near-infrared follow-up programme to ELAIS observations (Väisänen et al. 2002). In Fig. 23 measured fluxes are plotted against predicted ones for all 408 sources with reliable stellar identification and near-infrared magnitudes, showing the remarkable linearity and the small spread of the relation over a wide range of fluxes. Fig. 24 shows the histogram distribution of the measured/predicted flux ratio. Reducing the sample to the 300 sources with a S/N > 10 yields an average predicted/measured ratio of 1.0974 with a standard deviation of 0.0121. The difference between measured and predicted fluxes is significant at ∼8sigma, suggesting the presence of systematic effects in either the *IRAS* or *ISO* calibration process. Disentangling the effects leading to such a discrepancy would involve the reduction of a wide set of *IRAS*-detected sources observed by *ISO* using our method. Given the substantial amount of work that would be needed for this purpose, it was decided to simply correct (i.e. divide) our catalogue fluxes by a constant factor of 1.0974 to put them on the *IRAS* scale. However, while this choice was taken for the sake of compatibility of our results with studies adopting the *IRAS* flux scale (and particularly *IRAS*-based source counts and luminosity functions), this is not to indicate that the *IRAS* calibration is more secure that of *ISO*. In fact, results from data reduction of deep ISOCAM surveys in the Lockman Hole using the Lari Method (Fadda et al. 2004) favour the *ISO* calibration. On the basis of stellar atmosphere models applied to a smaller number of stars and deep multiband imaging, the authors find that model predictions agree with 15-μm fluxes determined following *ISO* calibration.

10 COMPARISON WITH PREVIOUS ANALYSES

The ELAIS 15-μm data set was already reduced in full as part of the preliminary analysis (hereafter PA Serjeant et al. 2000), while its S1 field was already reduced with a previous and less sophisticated version of the Lari Method (hereafter pre-final analysis, or pre-FA Lari et al. 2001). A comparison between these two catalogues and the FA catalogue is necessary in order to understand the merits and limitations of the different data-reduction procedures.

To compare FA with PA we used the PA catalogue by Serjeant et al. (2000) in its 1.3 version, calibrated using the recipe by Väisänen et al. (2002). Only high-reliability (rel = 2) sources from this catalogue were used, totalling 877. A cross-correlation between this source list and the FA catalogue, adopting a search radius of 6 arcsec,

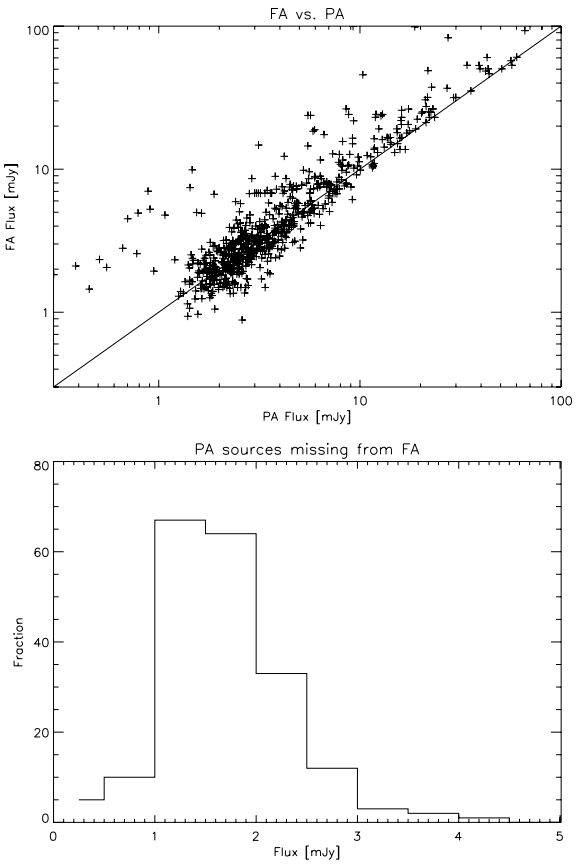

Figure 25. FA versus PA. Top panel shows the FA flux versus the PA flux for sources detected in both PA and FA. Bottom panel shows the histogram flux distribution of PA sources that are not detected in FA. In bottom panel, the brighest (16 mJy) PA source not detected by FA is not indicated. See text for details.

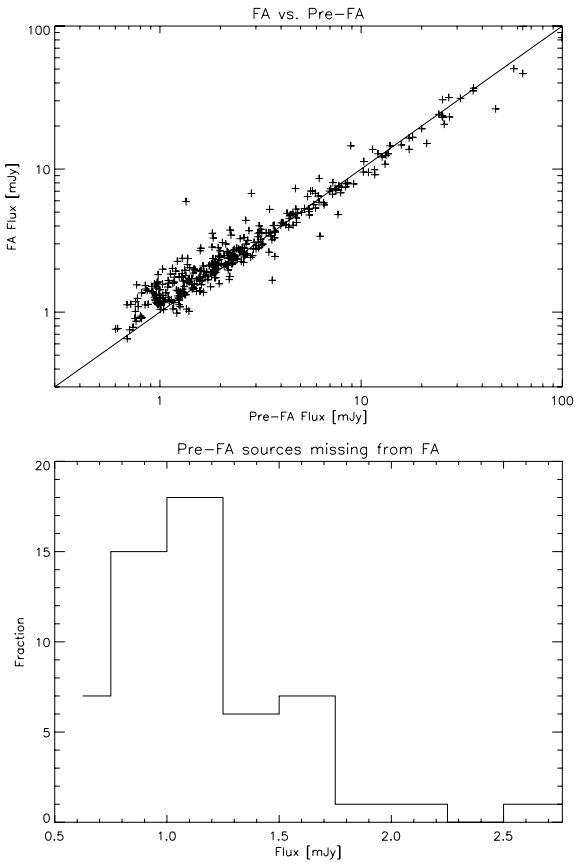

Figure 26. FA versus pre-FA. The top panel shows the FA flux versus the pre-FA flux for sources detected in both the pre-FA and the FA. The bottom panel shows the histogram flux distribution of pre-FA sources that are not detected in the FA. In the bottom panel, the brighest (4 mJy) pre-FA source not detected by the FA is not indicated. See text for details.

yielded 679, or 77.4 per cent, matches. The results of the cross-correlation are illustrated in Fig. 25.

A single very bright (16 mJy) PA source was not detected by FA, and probably arose from the detection, in PA, of two sources 18 arcsec apart that can only be associated with a single bright stellar source falling at the boundary between two rasters. Poor astrometry is thus the most likely cause for this. No PA source brighter than 2 mJy and missing from the FA was found to have a reliable optical association, suggesting that these sources, totaling 4 per cent of PA sources at this flux level, are spurious PA detections.

The FA/PA flux ratio is clearly dependent on the flux range under consideration. Its median value is 1.15 for sources brighter than 10 mJy, 1.02 for sources between 2 and 10 mJy and 0.86 for sources below 2 mJy. Considering that our photometric calibration is very accurate and holds over the whole covered flux range, this trend in FA versus PA fluxes seems to confirm that FA was substantially better at recovering the flux of sources at middle-to-faint levels, i.e. that the PA flux estimation process did not provide the desirable linearity. Most high FA/PA flux ratio outliers are either associated with sources which were unreasonably faint in the PA catalogue, well below the PA nominal flux limit, or with sources for which aperture photometry was carried out in FA. These latter sources were mostly extended to a greater or lesser degree, and for these the PA flux estimation process apparently led to a systematic flux underestimation.

On the basis of this comparison, PA was found to have a good (96 per cent) reliability down to 2 mJy, but its flux estimation process was found to be affected by a non-linearity bias at the 15 per cent level.

To compare FA with pre-FA in the S1 field we used the pre-FA catalogue by Lari et al. (2001). Only sources with high reliability and good flux measurements (rel = 0, as defined by La Franca et al. 2004) from this catalogue were used, totalling 406 sources. A cross-correlation between this source list and the FA catalogue, adopting a search radius of 6 arcsec, yielded 349, or 86.0 per cent, matches. The results of the cross-correlation are illustrated in Fig. 26.

Between the 57 pre-FA sources missing from FA, a single bright source (4 mJy) was found, and this was traced back to a human error when carrying out the FA interactive analysis process. Three other sources brighter than 2 mJy and eight more between 1.5 and 2 mJy were also found. The latter flux levels correspond to where the completeness is expected to start falling, as described by Gruppioni et al. (2002) for pre-FA and by Lari et al. (in preparation) for FA.

While the Lari Method as applied in FA generally provides improved reliability and completeness with respect to pre-FA, this is not to say that pre-FA sources not detected by FA are to be considered spurious. On the contrary, there is a variety of reasons connected with data reduction and catalogue construction for which pre-FA sources might be missing in FA. These reasons are essentially

connected with how sky maps were produced from reduced pixel time histories, how source extraction was carried out and the catalogue built. However, the most common cause for a pre-FA source being missing in the FA is the mosaicing technique implemented in the FA. While this provides several advantages, it projects all rasters making up a field on the same sky grid, whereas in the pre-FA all rasters were individually projected on a raster-centric grid. Then in both analyses source extraction was carried out estimating the S/N ratio of a source as its peak flux divided by the local noise, and the catalogue was built by cutting at S/N = 5. This leads to sources falling near the centre of a pixel having a greater probability of being detected with respect to those that fall near the boundary between two or more pixels. Therefore, the choice of a different grid in building maps between pre-FA and FA affects which faint sources finally appear in the two catalogues. Thus, the most common cause of the loss of a source is its having a pre-FA S/N ratio only marginally above 5 and its falling on the edge of a mosaic pixel, so that its FA S/N ratio drops below 5. This of course does not cast doubt on the reliability. Actually, upon visual inspection of the relevant portions of pixel time histories, all of the pre-FA sources missed by the FA appeared to be reliable. As a further demonstration, the fraction of optical identifications of these sources also appeared to be similar to the overall identification fraction for all sources over the same flux range.

While FA and pre-FA fluxes generally agree rather well, upon closer comparison a slight dependence of the FA/pre-FA flux ratio on the flux range under consideration is observed. The median FA/pre-FA flux ratio is 0.96 for sources brighter than 10 mJy, 1.01 for sources between 2 and 10 mJy and 1.08 for sources below 2 mJy. These systematic differences might be attributed to the shallower quality of pre-FA photometric calibration, which was determined on the basis of a smaller number of stars and without the help of near-infrared photometry.

On the basis of this comparison, the pre-FA and FA were found to have a very high reliability at all fluxes, while photometric calibration of the pre-FA was found to be lacking, as expected, at the 5 per cent level.

Following this analysis, a catalogue merging the reliable sources from the pre-FA and FA will be made available at http://astro.imperial.ac.uk/∼vaccari/elais. However, so as to not affect the significance of the completeness estimates derived from simulations (Lari et al. in preparation), we decided not to change the FA catalogue itself.

11 THE CATALOGUE

The ELAIS 15-μm Final Analysis Catalogue (v. 1.0) contains 1923 sources detected with a S/N ratio greater than 5 in the (RA-ordered) four fields S1, N3, N1 and N2, totalling an area of 10.85 deg^2. For each entry, the catalogue reports astrometric and photometric information, optical identification and a number of ancillary flags. The entries are as detailed in the following.

(i) **Name**: IAU source name constructed from RA and Dec.;

(ii) **RA (J2000)**: RA at epoch J2000 in both decimal and sexagesimal angular units.

Table 6. A sample portion of ELAIS 15-μm FA catalogue. Source IAU name, RA and Dec. at J2000 epoch in sexagesimal formats, total and peak flux, S/N ratio, astrometric and photometric errors, aperture flag. Note that a few columns described in the text were dropped for the sake of brevity.

Name	RA (J2000)	Dec. (J2000)	Total flux	Peak flux	S/N ratio	Astrometric error	Photometric error	Aperture flag
	hr min sec	deg min sec	mJy	μJy		arcsec	mJy	
ELAISC15_J143048.92+332830.08	14 30 48.9265	33 28 30.0837	1.2203	187.52	6.375	1.657	0.266	0
ELAISC15_J143053.24+333119.52	14 30 53.2422	33 31 19.5201	4.2931	649.40	18.421	0.944	0.691	0
ELAISC15_J143059.16+332215.08	14 30 59.1625	33 22 15.0859	3.0696	565.34	16.526	1.000	0.501	0
ELAISC15_J143112.10+325625.87	14 31 12.1003	32 56 25.8750	1.6166	166.20	5.266	1.834	0.392	0
ELAISC15_J143116.96+331957.83	14 31 16.9618	33 19 57.8304	3.1798	657.70	27.828	0.700	0.370	0
ELAISC15_J143116.99+332903.79	14 31 16.9954	33 29 3.7930	1.3766	296.39	12.327	0.980	0.189	0
ELAISC15_J143122.40+332036.07	14 31 22.4041	33 20 36.0725	2.2152	356.15	10.501	1.272	0.396	0
ELAISC15_J143123.57+330517.23	14 31 23.5781	33 5 17.2354	57.3303	11957.87	365.708	0.800	8.693	0
ELAISC15_J143125.36+331348.76	14 31 25.3603	33 13 48.7608	26.3799	1795.13	53.649	0.800	4.029	1
ELAISC15_J143131.33+330143.80	14 31 31.3313	33 1 43.8084	6.7570	958.24	30.352	0.800	1.048	0
ELAISC15_J143135.38+333224.62	14 31 35.3831	33 32 24.6235	0.8125	122.88	5.278	1.477	0.178	0
ELAISC15_J143135.47+325456.62	14 31 35.4741	32 54 56.6245	1.6331	301.73	9.053	1.376	0.306	0
ELAISC15_J143137.69+325453.32	14 31 37.6931	32 54 53.3249	2.5355	495.93	14.764	1.062	0.421	0
ELAISC15_J143138.44+332808.85	14 31 38.4461	33 28 8.8581	1.4309	274.79	7.864	1.483	0.283	0
ELAISC15_J143140.70+330316.82	14 31 40.7051	33 3 16.8265	3.6781	747.97	23.415	0.831	0.579	0
ELAISC15_J143142.01+331003.66	14 31 42.0114	33 10 3.6686	1.6108	269.70	8.391	1.433	0.310	0
ELAISC15_J143143.08+325301.48	14 31 43.0892	32 53 1.4801	1.2484	249.18	5.679	1.762	0.290	0
ELAISC15_J143143.58+333200.05	14 31 43.5875	33 32 0.0592	2.4374	386.42	14.690	1.065	0.405	0
ELAISC15_J143143.69+330133.41	14 31 43.6981	33 1 33.4117	2.4854	393.08	12.373	1.166	0.427	0
ELAISC15_J143143.86+333119.96	14 31 43.8619	33 31 19.9622	0.9966	200.88	6.450	1.647	0.216	0
ELAISC15_J143149.61+330212.86	14 31 49.6144	33 2 12.8683	2.7584	404.89	14.698	1.064	0.458	0
ELAISC15_J143155.98+330138.26	14 31 55.9881	33 1 38.2622	1.5529	263.79	7.163	1.558	0.320	0
ELAISC15_J143156.34+325138.33	14 31 56.3402	32 51 38.3395	3.8175	811.95	17.343	0.975	0.619	0
ELAISC15_J143159.54+325439.10	14 31 59.5441	32 54 39.1004	1.3582	232.94	6.381	1.656	0.296	0
ELAISC15_J143201.02+331525.84	14 32 1.0279	33 15 25.8460	2.0073	342.84	9.346	1.353	0.372	0

(iii) **Dec. (J2000)**: Declination at epoch J2000 in both decimal and sexagesimal angular units.

(iv) **Total flux**: source total flux obtained from autosimulation or aperture photometry [see 'Aperture' in part (ix)], expressed in mJy.

(v) **Peak flux**: source peak flux measured on unreconstructed maps, expressed in μJy pixel^{-1}.

(vi) **S/N**: S/N ratio measured on unreconstructed maps.

(vii) **Astrometric error**: astrometric error as determined from equation (6).

(viii) **Photometric error**: photometric error as determined from equation (7).

(ix) **Aperture**: aperture photometry flag, 0 for sources whose flux was estimated through autosimulation and 1 for sources on which aperture photometry was preferred (see Section 4).

(x) **Optical ID**: optical identification as described in Section 6. S stands for star, G for galaxy and * for unidentified source. A further D flags a particularly dubious (non-)identification.

A sample of the catalogue, which is available at http://astro.imperial.ac.uk/∼vaccari/elais, is shown in Table 6. Some of the data on the sources are also contained within the ELAIS band-merged catalogue by Rowan-Robinson et al. (2004), which is available at http://astro.imperial.ac.uk/Elais/Data_release.

12 CONCLUSIONS

A technique for ISOCAM/ISOPHOT data reduction, the Lari Method, was variously refined and applied to ELAIS 15-μm observations. The mathematical model for the behaviour of the detector is the same as originally presented in Lari et al. (2001), but thanks to various improvements, and particularly to a new graphical user interface, the method is now more robust and, most importantly, quicker and easier to apply to large data sets. Its application, in the new form, to the four fields composing the data set [including a re-reduction of S1 observations already presented in Lari et al. (2001)] has produced a catalogue of 1923 sources spanning the 0.5–100 mJy range, detected with a S/N ratio greater than 5 over a total area of 10.85 deg^2. Optical identification of 15-μm sources has been carried out on heterogeneous optical and near-infrared imaging material, allowing one to determine a robust association for about 85 per cent of the sources and identify 22 per cent of them as bona fide stars, further demonstrating the reliability of our data-reduction process.

The evaluation of the quality of the catalogue has been carried out through both accurate simulations and multiwavelength identification. The astrometric accuracy is of order 1 arcsec in both RA and Dec. for S/N $>$ 10, while it increases up to about 2 arcsec in both RA and Dec. for S/N $\sim$ 5, and somewhat better for sources detected in higher redundancy sky regions. The photometric accuracy is estimated to be below 25 per cent over the whole range of fluxes and redundancy levels probed by our catalogue, and better than 15 per cent for S/N $>$ 10 sources.

The comparison of measured stellar fluxes with fluxes estimated on the basis of stellar atmosphere models calibrated on *IRAS* data and on near-infrared photometry allowed an *IRAS*/*ISO* relative photometric calibration. An *IRAS*/*ISO* relative calibration factor of 1.0974 $\pm$ 0.0121 was determined, shedding doubts on the goodness of the two independently determined calibrations at the 10 per cent level. Owing to the lack of a simple way to identify error sources in *IRAS* and/or *ISO* calibratioon process, it was decided to put our catalogue on the more commonly used *IRAS* flux scale.

A comparison of the catalogue with results from previous analyses by Serjeant et al. (2000) and Lari et al. (2001) confirmed on one hand its high quality, particularly with respect to reliability, and on the other the improvements to the data-reduction technique, particularly with respect to photometric calibration.

In a forthcoming paper (Lari et al. in preparation) completeness estimates and extragalactic source counts from this catalogue will be presented, covering the crucial flux range 0.5–100 mJy between ISOCAM 15-μm deep surveys and the *IRAS* all-sky Survey.

ACKNOWLEDGMENTS

This paper is based on observations with *ISO*, an ESA project with instruments funded by ESA Member States (especially the PI countries: France, Germany, the Netherlands and the UK) and with the participation of ISAS and NASA.

This work was partly supported by the 'POE' EC TMR Network Programme (HPRN-CT-2000-00138).

REFERENCES

Aussel H., Cesarsky C. J., Elbaz D., Starck J. L., 1999, A&A, 342, 313
Bertin E., Dennenfeld M., Moshir M., 1997, A&A, 323, 685
Cesarsky C. J. et al., 1996, A&A, 315, L32
Désert F. X. et al., 1999, A&A, 342, 363
Elbaz D. et al., 1999, A&A, 351, 37
Fadda D., Lari C., Rodighiero G., Franceschini A., Elbaz D., Cesarsky C., Perez-Fournon I., 2004, A&A, 427, 23
Franceschini A., Danese L., Toffolatti L., de Zotti G., 1988, MNRAS, 233, 175
Genzel R., Cesarsky C. J., 2000, ARA&A, 38, 761
Gonzalez-Solares E. et al., 2005, MNRAS, submitted, astro-ph/0402406
Gregorich D. T., Neugebauer G., Soifer B. T., Gunn J. E., Herter T. L., 1995, AJ, 110, 259
Gruppioni C., Lari C., Pozzi F., Zamorani G., Franceschini A., Oliver S., Rowan-Robinson M., Serjeant S., 2002, MNRAS, 335, 831
Hacking P., Houck J. R., Condon J. J., 1987, ApJ, 316, 15
Høg E. et al., 2000, A&A, 355, 27
Kessler M. F. et al., 1996, A&A, 315, L27
La Franca F. et al., 2004, AJ, 127, 3075
Lari C. et al., 2001, MNRAS, 325, 1173
Lari C., Vaccari M., Rodighiero G., Fadda D., Gruppioni C., Pozzi F., Franceschini A., Zamorani G., 2003, ESA SP-511, 349
Lejeune T., Cuisinier F., Buser R., 1998, A&ASS, 130, 65
Lemke D. et al., 1996, A&A, 315, L64
Lonsdale C. J., Hacking P. B., Conrow T. P., Rowan-Robinson M., 1990, ApJ, 358, 60
Lonsdale C. J. et al., 2003, PASP, 115, 897
McMahon R. G., Walton N. A., Irwin M. J., Lewis J. R., Bunclark P. S., Jones D. H., 2001, New Astron. Rev., 45, 97
Neugebauer G. et al., 1984, ApJ, 278, L1
Okumura K., 1998, ISOCAM PSF Report, available at http://www.iso.vilspa.esa.es/users/expl_lib/CAM_list.html
Okumura K., 2000, ISOCAM Field Distortion Report, available at http://www.iso.vilspa.esa.es/users/expl_lib/CAM_list.html
Oliver S., 2000, MNRAS, 316, 749
Omont A. et al., 1999, A&A, 348, 755
Ott S., Gastaud R., Ali B., Delaney M., Miville-Deschênes M.-A., Okumura K., Sauvage M., Guest S., 2001, ASP Conf. Ser., 238, 170
Pozzi F. et al., 2003, MNRAS, 343, 1348
Rodighiero G., Lari C., Franceschini A., Gregnanin A., Fadda D., 2003, MNRAS, 343, 1155
Rodighiero G., Lari C., Fadda D., Franceschini A., Elbaz D., Cesarsky C., 2004, A&A, 427, 773
Rowan-Robinson M. et al., 1984, ApJ, 278, 7
Rowan-Robinson M. et al., 1991, Nat, 351, 719
Rowan-Robinson M. et al., 2004, MNRAS, 351, 1290
Sato Y. et al., 2003, A&A, 405, 833

Saunders W., Frenk C., Rowan-Robinson M., Lawrence A., Efstathiou G., 1991, Nat., 349, 32
Schlegel D. J., Finkbeiner D. P., Davis M., 1998, ApJ, 500, 525
Serjeant S. et al., 2000, MNRAS, 316, 768
Shibai H., 2004, AdSpR, 34, 589
Soifer B. T. et al., 1984, ApJ, 278, 71
Soifer B. T., Houck J. R., Neugebauer G., 1987, ARA&A, 25, 187
Starck J. L., Aussel H., Elbaz D., Fadda D., Cesarsky C., 1999, A&AS, 138, 365
Väisänen P. et al., 2002, MNRAS, 337, 1043

This paper has been typeset from a TEX/LATEX file prepared by the author.